

A mechanistic model and experiments on bedrock incision and channelization by rockfall

Alexander R Beer¹, Jade N. Fischer², Thomas P Ulizio³, Zewei Ma⁴, Zhongheng Sun⁵, and Michael P Lamb³

¹University of Tübingen

²Massachusetts Institute of Technology

³California Institute of Technology

⁴University of Illinois at Urbana-Champaign

⁵College of Marine Science and Technology, China University of Geosciences

January 30, 2024

A mechanistic model and experiments on bedrock incision and channelization by rockfall

A. R. Beer^{1,2*}, J. N. Fischer^{2,3}, T. P. Ulizio¹, Z. Ma^{2,4}, Z. Sun^{2,5}, and M. P. Lamb²

¹University of Tübingen, D-72076 Tübingen, Germany

²California Institute of Technology, Pasadena, California 91125, USA

³Massachusetts Institute of Technology

⁴University of Illinois Urbana-Champaign

⁵College of Marine Science and Technology, China University of Geosciences, Wuhan 430074, China

*Corresponding author: Alexander Beer (alexander.beer@uni-tuebingen.de)

Key Points:

- Rockfall can erode rocky hillslopes even below the angle of repose
- Grain size has a dominant effect on impact abrasion; slope is of minor importance
- Topographic steering of grains results in self-formed bedrock channels

Abstract

Rockfall and rock avalanches are common in steep terrain on Earth and potentially on other planetary bodies such as the Moon and Mars. Since impacting rocks can damage exposed bedrock as they roll and bounce downhill, rockfall might be an important erosive agent in steep landscapes, even in the absence of water. We developed a new theory for rockfall-driven bedrock abrasion using the ballistic trajectories of rocks transported under gravity. We calibrated this theory using laboratory experiments of rockfall over an inclined bedrock simulant. Both the experiments and the model demonstrate that bedrock hillslopes can be abraded by dry rockfall, even at gradients below the angle of repose, depending on the bedrock roughness. Feedbacks between abrasion and topographic steering of rockfall can produce channel-like forms, such as bedrock chutes, in the absence of water. Particle size has a dominant influence on abrasion rates and runout distances, while hillslope angle is of comparatively minor influence. Rockfall transport is sensitive to bedrock roughness; terrain with high friction angles can trap rocks creating patches of rock cover that affect subsequent rockfall pathways. Our results suggest that dry rockfall can play an important role in eroding and channelizing steep, rocky terrain on Earth and other planets, such as crater degradation on the Moon and Mars.

37 Plain language summary

38 Rockfall is common on Earth and other planets. Falling rocks bounce down rocky slopes and
39 likely also erode them. However, it has not been explored how erosive this process is, nor what
40 landforms it might generate. We developed a numerical model for this erosion process and
41 calibrated it with experiments of dry grains hopping down an inclined erodible surface. Both
42 experiments and modeling showed that bedrock erosion from rockfall can happen, even on
43 relatively low-gradient hills. Small hollows were carved by rockfall, which over time coalesced
44 into larger troughs that captured the path of subsequent rocks. This process led to a self-
45 enhancing feedback that produced a bumpy surface with rocky chutes. Rock size had a larger
46 effect on erosion amounts than the steepness of the hill. Our work suggests that dry rockfall
47 can play an important role in the evolution of mountain slopes on Earth and craters on the
48 Moon and other planets.

49

50 1 Introduction

51 Rockfall is a ubiquitous, gravitational-driven process in steep terrain. There is evidence
52 for dry rockfall and rock avalanches on Earth (e.g., Stock et al., 2013), as well as on the Moon
53 and Mars (Bickel et al., 2020a, 2020b; Kumar et al., 2013; Vijayan et al., 2022; Ward et al., 2011;
54 Figure 1A to D). There has been a wealth of research into its preconditioning and cause, both on
55 vertical walls and on mountain slope topography (e.g., Benjamin et al., 2020; D'Amato et al.,
56 2016; Frayssines and Hantz, 2006; Grenon and Hadjigeorgiou, 2008; Matasci et al., 2018;
57 Messenzehl et al., 2017; Wieczorek et al., 1992; Williams et al., 2019). Generally, lithological
58 and exhumation-induced rock fracture, climate, hydrology, and earthquakes are triggers for
59 rock mass release (André, 1997; Collins and Stock, 2016; Guerin et al., 2013; Hales and Roering,
60 2007; Leith et al., 2014; Mackey and Quigley, 2014; Moore et al., 2009). Also, sediment mass
61 routing following rockfall on steep topography has been accounted for in terms of block-runout
62 and rock avalanching (Dade and Huppert, 1998; Volkwein et al., 2011), in combination with
63 debris flows and fluvial bedload transport (Mergili et al., 2020; Montgomery and Dietrich, 1994;
64 Shugar et al., 2021). Dry rockfall and rock avalanches are typically studied due to their
65 substantial hazard potential. However, they also can be significant agents of erosion, mass
66 transport, and landscape change (Loye et al., 2012; Delannay et al., 2017; Sass and Krautblatter,
67 2007). Yet, we currently lack mechanistic modeling and experimental constraints on bedrock
68 erosion by rockfall.

69 Discrete, dry rockfall in physical experiments was shown to erode sloping bedrock
70 surfaces even below the angle of repose (Mokudai et al., 2011; Sun et al., 2021). Rockfall
71 erosion is also supported by observations of boulder tracks (Bickel et al., 2020a, 2020b; Kumar
72 et al., 2013). The impact energy of large rocks that break free from cliffs is substantial
73 (Blackwelder, 1942; Le Roy et al., 2019; Rapp, 1960), and their momentum leads to increased
74 runout distances compared to the smaller grain sizes (Kokelaar et al., 2017; Volkwein et al.,
75 2011). Bedrock abrasion theory suggests that bedrock erosion should scale linearly with impact
76 energy and inversely with the square of rock tensile strength (Beer and Lamb, 2021; Sklar and
77 Dietrich, 2004). So, given abundant rockfall sources in rocky topography, abrasion of bedrock

78 along the rockfall traverse could be an important process in the topographic evolution of steep
79 terrain (Beer et al., 2019; Sun et al., 2021), despite not being included in most landscape
80 evolution models.

81 Landforms developed by water-rich rivers and debris flows have received far better
82 study owing to their importance on Earth and they are known to produce channels. In contrast,
83 most previous work on dry granular flows has focused on flow over loose granular substrates,
84 like rock avalanches over talus slopes or grain flows on the front of a sand dune (e.g., Delannay
85 et al., 2017; Selby, 1982). Granular flows tend to spread laterally (Lajeunesse et al., 2004),
86 creating relatively smooth convex lobes, such as grain flows on the avalanche face of a wind
87 dune. The subtle levees and depressions in-between lobes tend to be filled in or diffused away
88 by subsequent avalanches (McDonald and Anderson, 1996). Dry granular flows also tend to
89 cease movement at relatively steep angles of repose, which is around 35–45° for most grains,
90 forming a cone or planar talus slope (Figures 1E and G; Delannay et al., 2017; Kirkby and
91 Statham, 1975; Sass and Krautblatter, 2007; Selby, 1982). Similar angles for dry granular flow
92 deposits have been measured on Mars (Atwood-Stone and McEwen, 2013; Dickson et al.,
93 2007). The generally smooth and steep topography from dry flows over loose substrates
94 contrasts sharply with the channel-like landforms developed in some steep rocky terrain, such
95 as bedrock chutes (Figures 1C and D; Ward et al., 2011). This contrast has fueled the idea that
96 water is needed to develop channelized forms, particularly at slopes less than the angle of
97 repose for dry avalanches (e.g., Howard, 2007).

98 The mechanics of how flowing water produces channels is relatively well understood.
99 Water follows the steepest slope, such that the topography funnels the flow, causing erosion
100 rates to increase, which, in turn, causes further channelization (Horton, 1945). It is unclear if a
101 similar feedback can occur for dry rockfall. While dry granular flows can be focused down pre-
102 existing topography (Pelletier et al., 2008), dispersive pressures due to grain-grain and grain-
103 bed collisions cause granular flows to spread laterally (e.g., Lajeunesse et al., 2004; Figure 1G),
104 rather than to focus and entrench. However, Sun et al. (2021) showed in an experiment that dry
105 rockfall traversing a bedrock substrate can form channelized landforms. The strong substrate
106 allowed for persistent topographic forms over many rockfall events, which steered rockfall into
107 preferred pathways. Thus, similar to fluvial incision, rockfall was funneled into proto-channels,
108 enhancing erosion there (Figure 1H) and allowing for further entrenchment. Another
109 experiment that produced chutes by dry flows used a very light and fine-grained sediment
110 substrate under high humidity, which provided cohesive strength between grains (Shinbrot et
111 al., 2004). Rockfall over a relatively smooth bedrock substrate can traverse relatively low-
112 sloping terrain due to low friction angles (DiBiase et al., 2017; Sun et al., 2021), which may help
113 explain channel-like landforms below the angle of repose on the Moon and Mars in the absence
114 of water (Conway et al., 2015; Dickson et al., 2007; Heldmann and Mellon, 2004).

115 Here we develop theory and a numerical model for abrasion by rolling and bouncing
116 rocks over a bedrock bed in order to better understand the role of rockfall in landscape
117 denudation and landform development. We calibrated and evaluated the model against
118 physical experiments of dry rockfall traversing a planar and tilted bedrock slope, where we used
119 polyurethane foam as a bedrock simulant, similar to Sun et al. (2021). We used the model to

120 answer whether rockfall can form channelized landforms, and the effect that hillslope angles
121 and rockfall sizes have on rockfall erosion rates.

122 **2 Dry Grain Abrasion Model (DGAM)**

123 **2.1 Grain trajectories**

124 We develop a dry grain abrasion model (DGAM), which tracks discrete rockfall events,
125 including grain trajectories and abrasion over a gridded 2.5D digital elevation model (DEM with
126 no 3D overhangs), built out of X, Y, Z -coordinates with slopes θ_{cell} [°] and cellsize d_{cell} [m]
127 (setup in Figure 2A; scheme and workflow in the Supplemental Information and Table S1; see
128 notation section). For simplicity, we model only one rockfall grain size and set d_{cell} equal to the
129 grain diameter d_{grain} [m]. Each grain of mass m_{grain} [kg] is released from the upstream
130 boundary of the model domain with initial variable values (grain deflection velocity, $v_{out,0}$
131 [m/s], absolute grain deflection angle, $\alpha_{out,0}$ [°], and grain hop length, $l_{hop,0}$ [m]), in one of the
132 D8 grid directions (parameter ξ_0 ; i.e. deflection to all adjacent neighbor cells). By having these
133 variables drawn from an intended distribution, this procedure ensures controllable randomness
134 to the first impacts.

135 Inside the model domain, grains hop over multiple cells following classical mechanics
136 (ballistics) along a tilted plane. For a defined grain impact cell i (with coordinates X, Y, Z_i), we
137 calculate the incoming grain's trajectory from its original deflecting cell (X, Y, Z_{i-1}) as grain hop
138 length $l_{hop,i-1}$ along the direction ξ_{i-1} , as the distance between both cell's coordinates (ΔXY
139 is the horizontal distance, and ΔZ is the vertical distance between both cells)

$$140 \quad l_{hop,i-1} = \sqrt{\Delta XY^2 + \Delta Z^2} \quad (1)$$

141 The hop time, $t_{hop,i-1}$ [s], of this trajectory is based on the grain's original deflection variables
142 $v_{out,i-1}$ and $\sin \alpha_{out,i-1}$, as well as on gravitational acceleration, a_{grav} [m/s²):

$$143 \quad t_{hop,i-1} = v_{out,i-1} \sin \alpha_{out,i-1} + \frac{\sqrt{(v_{out,i-1} \sin \alpha_{out,i-1})^2 + 2a_{grav}\Delta Z}}{a_{grav}} \quad (2)$$

144 Grain velocity at the cell impact, $v_{in,i}$ [m/s], and grain impact angle, $\alpha_{in,i}$ [°], then are:

$$145 \quad v_{in,i} = \sqrt{(v_{out,i-1} \cos \alpha_{out,i-1})^2 + (v_{out,i-1} \sin \alpha_{out,i-1} - a_{grav} t_{hop,i-1})^2} \quad (3)$$

$$146 \quad \alpha_{in,i} = \arcsin \frac{v_{out,i-1} \cos \alpha_{out,i-1}}{v_{in,i}} \quad (4)$$

147 After an impact (i.e., along the next trajectory direction, ξ_{i+1}), the grain trajectory
148 follows a probabilistic direction-sampling based on weighted downslope gradients in the
149 proximity of the impact cell (DiBiase et al., 2017; Dorren et al., 2004). This procedure is
150 intended to account for natural stochasticity of the rebounds due to grain inertia, grain shape,
151 and surface roughness (cf. Volkwein et al., 2011).

152 The model can be operated in two modes to assess frictional losses due to impacts with
153 the bed. In the pure grain hop mode (mode I), grain kinetic energy loss from impacts is
154 expressed in grain velocity reduction by means of a shock term, κ_{shock} [1/m] (Quartier et al.,
155 2000),

$$156 \quad v_{out,i} = v_{in,i} - \kappa_{shock} v_{in,i}^2 \Delta t \quad (5a)$$

157 with $v_{out,i}$ [m/s] is the deflection grain velocity, and Δt [s] is an impact time, which we assume
 158 to be 0.1 s (DiBiase et al., 2017; Gabet and Mendoza, 2012). In mode II, impact energy loss also
 159 includes sliding and rolling friction based on a modified Coulomb friction law (DiBiase et al.,
 160 2017; Gabet and Mendoza, 2012),

$$161 \quad v_{out,i} = v_{in,i} - a_{grav} (\sin \theta_{cell,i} - \tan \Phi_{surf,i} \cos \theta_{cell,i}) - \kappa_{shock} v_{in,i}^2 \Delta t \quad (5b)$$

162 which includes the dynamic surface friction angle, $\Phi_{surf,i}$ [°] between grains and the surface,
 163 accounting for microtopography. Following previous work (DiBiase et al., 2017; Gabet and
 164 Mendoza, 2012), we treat this slope as an exponential probability distribution

$$165 \quad \Phi_{surf,i} = \arctan\left(\frac{1}{\tan \bar{\mu}_{surf}} e^{-\frac{\tan \mu_{eff}}{\tan \bar{\mu}_{eff}}}\right) \quad (6)$$

166 of the effective friction angle μ_{eff} [°]. The grain's deflection angle $\alpha_{out,i}$ [°] is assumed to be
 167 the reflection angle of $\alpha_{in,i}$ on the local cell slope $\theta_{cell,i}$ [°] in direction ξ_i

$$168 \quad \alpha_{out,i} = \alpha_{in,i} - 2\theta_{cell,i} \quad (7)$$

169 The location of the next impact (X, Y, Z_{i+1}) then is determined by an iterative process.
 170 The grain's trajectory heights Z_{traj} [m] are calculated relative to the traversed cell boundaries
 171 $Z_{cell.boundary}$ [m] along the grain's trajectory direction ξ_i

$$172 \quad Z_{traj} = \tan \alpha_{out} (n_{cells} + 0.5) \frac{d_{cell}}{2} - \frac{a_{grav}}{2v_{out,i}^2 \cos^2 \alpha_{out,i}} \left(\frac{d_{cell}}{2}\right)^2 \quad (8)$$

173 for a number of n_{cells} until $Z_{traj} < Z_{cell.boundary}$. Then (X, Y, Z_{i+1}) is defined as the last cell
 174 that could not be traversed by the grain, and $l_{hop,i}$ is calculated in between (X, Y, Z_i) and
 175 (X, Y, Z_{i+1}) (Equation 1). The grain's hop height $h_{hop,i}$ [m] is the maximum of the vertical
 176 distances between traversed cell boundaries and trajectory heights, i.e. $\max(Z_{traj} -$
 177 $Z_{cell.boundary})$. The trajectory procedure is repeated until the grain leaves the model domain or
 178 comes to rest (Table S1). If a grain has too low deflection velocity, v_{out} , or too low deflection
 179 angle, α_{out} , to cross the next cell boundary, it is deposited at the current cell. We assume a
 180 resting particle is subsequently set in motion from being hit by a mobile grain, drawing
 181 randomly from the grain entrance variable values discussed above. However, if a grain is in a
 182 depression with neighboring cells higher than two grain sizes, we assume the grain stays there
 183 and acts as cover that protects the bedrock from abrasion.

184

185 2.2 Bedrock abrasion and morphodynamics

186 The amount of bedrock abrasion of a cell, $w_{cell,i}$ [m], due to a single grain impact is
 187 calculated as:

$$188 \quad w_{cell,i} = k_{ero} \frac{0.5m_{grain}v_{in,i}^2}{d_{cell}^2} = k_{ero} \frac{\epsilon_{kin,i}}{d_{cell}^2} \quad (9)$$

189

$$190 \quad v_{in,n,i} = \cos \theta_{cell,i} v_{in,i} \sin \alpha_{in,i} \quad (10)$$

191 based on a bedrock erosion efficiency factor, k_{ero} (i.e., grain erosivity, [m^3/J]). To conserve
 192 mass, the erosion amount, $w_{cell,i}$, is assessed in the vertical direction since the cell area in our
 193 calculations is measured on a horizontal grid. The surface-normal component of the kinetic
 194 impact energy, $\varepsilon_{kin,n}$ [J], results from the surface-normal component of the grain impact
 195 velocity, $v_{in,n}$ [m/s]. The velocity component accounts for impact-induced fracturing causing
 196 wear, instead of surface-parallel gouging (cf. Sun et al., 2021). For steeper slopes, its value
 197 decreases compared to the approximation of a vertical impact velocity that is commonly used
 198 in fluvial abrasion theory (Beer and Lamb, 2021; Beer and Turowski, 2021; Engel, 1978; Sklar
 199 and Dietrich, 2004). While the actual geometry of the impact event depends on local
 200 parameters like grain shape and bedrock roughness that are not explicitly included in the
 201 model, the model is calibrated with experiments (below) and thus these local geometric effects
 202 are incorporated into the empirical model parameters.

203 The DGAM model allows the user to switch off abrasion (Equation 9), since it is
 204 decoupled from frictional losses (Equation 5). This option enables process-independent model
 205 assessment like varying grain sizes or hillslope angle. Accounting for abrasion (Equation 9)
 206 results in evolving hillslope topography that influences grain impact energy ε_{kin} (via modified
 207 hop time t_{hop} , which drives impact velocity v_{in} ; Equation 3), and alters the local slope gradient
 208 around each cell. This again affects the subsequent direction of deflecting grains (parameter ξ),
 209 which can result in topographic steering feedback. Application of the model requires inputs of
 210 initial grain entrance variables ($v_{out,0}$, $\alpha_{out,0}$ and $l_{hop,0}$) and the bedrock erosion factor, k_{ero} ,
 211 per model cell. The grain impact shock term, κ_{shock} , is calibrated as described below, but could
 212 be adjusted for specific situations (e.g., varying grain shape).

213

214 **3. Experimental Setup and Model Application**

215 We conducted two sets of experiments (Table 1) to generate grain trajectory and
 216 abrasion data, and used this data to calibrate the DGAM model. The first set consisted of five
 217 large-scale experiments with an erodible foam substrate that evolved during the experiments
 218 due to abrasion from dry rockfall. We refer to these as *erodible-bed experiments* (EB). The
 219 erodible-bed experiments had different inlet conditions, hillslope gradients, and particle sizes
 220 to test the model performance relative to these variables. The experiments of the second set
 221 were of smaller scale, did not vary the inlet nor erode the bed, and were used to evaluate grain
 222 trajectories as a function of bed slope. We refer to these as *fixed-bed experiments* (FB).

223

224 **3.1. Erodible-bed experiments**

225 We ran five erodible-bed experiments (EB, Table 1; more details in Table S2). These
 226 experiments were not designed to replicate or reproduce particular rockfall and hillslope
 227 topography, but to provide data on grain trajectories, bedrock abrasion, and morphodynamic
 228 feedback for model comparison. Erodible-bed experiment 1 (i.e., EB1) was conducted using a
 229 2.2 m long, 0.76 m wide test section using large river cobbles on a relatively shallow sloping
 230 bed ($\theta_{slope} = 16.7^\circ$). The detailed experimental setup and some results from experiment EB1

231 were previously described in Sun et al. (2021). These observations include the ability of rockfall
 232 to run out over low gradients and to focus, resulting in channelized landforms through
 233 topographic steering. Here, we use data from *EB1* to help evaluate DGAM and to compare
 234 results from four additional erodible-bed experiments and six fixed-bed experiments, as
 235 detailed below.

236 The four new erodible bed experiments (*EB2 – EB5*) were conducted in a different but
 237 comparable facility as *EB1*. We used a tilting flume, 4.5 m long and 0.65 m wide, filled with a
 238 block of smooth, homogeneous polyurethane (PU) foam, which acted as a highly-erodible
 239 substitute for bedrock (Scheingross et al., 2014; Figures 2B, C). Each experiment (including *EB1*)
 240 used the same type of foam with a density of 0.06t/m^3 , a tensile strength of $\sigma_{foam} =$
 241 0.32MPa , and a Young's Modulus of 3.92MPa . This foam has been shown previously to
 242 produce realistic erosional morphologies through abrasion by grain impacts in both air and
 243 water (Scheingross et al., 2014; Sun et al., 2021). Moreover, the foam erodibility follows the
 244 same scaling law with tensile strength as bedrock, supporting it as an experimental analog to
 245 natural rock (Beer and Lamb, 2021; Lamb et al., 2015). The erodibility framework holds over
 246 several orders of magnitude both in impactor energy and impact abrasion (Beer and Lamb,
 247 2021), indicating that these laboratory experiments can be scaled to natural cases of larger
 248 impact energies and real bedrock using the relative erodibilities in a scaling factor.

249 The variables that changed between our experiments were the inlet design for the
 250 grains to enter the flume, grain size/shape properties, and the flume slope (Table 1).
 251 Experiment *EB1* used rounded granitic grains (density of 2.75 t/m^3) with a median grain
 252 diameter of $d_{grain} = 0.061\text{m}$; experiments *EB2-EB4* used medium-sized and rounded andesitic
 253 grains ($d_{grain} = 0.023\text{m}$ and 0.03m , respectively; grain density of 2.33t/m^3 ; Figure 2D); and
 254 *EB5* used 0.015m angular granite grains. The initial slope of the planar foam bed was $\theta_{slope} =$
 255 16.7° for *EB1*, 19.5° for *EB2-EB4* and 35.0° for *EB5*. The inlet for rockfall spanned the width of
 256 the flume for experiments *EB1*, *EB2* and *EB5*, but was constricted to 0.2m width in the flume-
 257 center for experiments *EB3* and *EB4* (Table S2).

258 The experiments were designed such that the surface friction angle of the grains on the
 259 foam $\Phi_{surf} [^\circ]$ was similar to the slope θ_{slope} of the planar foam bed at the beginning of the
 260 experiment (Table 1). This design was intended to allow grains to be intermittently mobile even
 261 when patches of static grains were deposited on the bed. The grain's pocket friction angle,
 262 $\Phi_{pocket} [^\circ]$ (corresponding to the angle of repose of a grain pile) was measured following
 263 previous work (Prancevic and Lamb, 2015; Sun et al., 2021), whereby we glued grains of like
 264 size and angularity on a planar board. Then a loose grain was placed on this surface, the board
 265 was slowly tilted until the grain was mobilized, and the tilting angle was reported as the pocket
 266 friction angle. The process was repeated for ~ 100 different grains selected at random and
 267 placed at random on the board. We also repeated this process for grains placed on the planar
 268 foam board, which we report as the mean surface friction angle, $\Phi_{surf} [^\circ]$. Grains should be
 269 highly mobile when their friction angle is lower than the topographic slope (DiBiase et al.,
 270 2017), which was the case for all of our experiments with grains traversing the smooth foam
 271 bedrock. However, this mobility transiently changed during the experiments due to the growth
 272 of topographic bedrock roughness and due to static patches of grains that were more difficult

273 to traverse (i.e., $\Phi_{pocket} > \Phi_{surf}$; Table 1). Although we achieved high mobility in the
274 experiments through relatively round grains and smooth foam topography, low surface friction
275 angles are also expected in natural settings with angular rockfall grains that are much larger
276 than the bedrock topographic roughness (DiBiase et al., 2017; Sun et al., 2021). In other words,
277 modeling multi-meter scale boulders in the laboratory is not feasible, so we created similar
278 particle dynamics by lowering the surface friction angle through particle roundness rather than
279 by larger grain size.

280 Each experiment started with a new block of planar, smooth foam (Figure 2C). Dry
281 grains were introduced at the upslope end of the flume at a steady rate from an auger
282 sediment feeder. The feed rate was slow enough (250 – 1'550 grains/minute), so grains
283 entered and traversed the flume individually, with minimal grain-grain interactions. Particles
284 traversed a board with pegs spaced at 0.05m to spread the grains across the inlet. The flume
285 had rigid vertical walls that reflected grains towards the center of the test section, mimicking
286 grains exiting and entering the domain under an infinitely wide scenario. Each experiment
287 lasted for several hours of runtime, in which 5 – 22 t of sediment traversed the test section
288 (Table 1; details in Table S2).

289 Grain trajectories were recorded using high-speed cameras with fisheye lenses
290 (GRASHOPPER, set to 160 frames/s) at three lateral positions along the flume (Figure 2B) and
291 one camera from top. We rectified and cut the distorted fisheye-lens pictures, converted them
292 to black and white, and scaled their dimensions by scale bars attached to the flume walls in the
293 photos. Then we applied particle imaging velocimetry (PIV) to measure grain trajectories using
294 Python-based software packages (OpenCV and TrackPy; Python, 2021) and calculated grain
295 trajectory metrics. For the side-view cameras, these metrics were grain impact and deflection
296 velocities (v_{in} and v_{out}), impact and deflection angles (α_{in} and α_{out}), hop heights, and hop
297 lengths (h_{hop} and l_{hop} ; Figure 2B; Table 1; Table S2), which we calculated perpendicular to the
298 foam surface from grain traces through subsequent pictures. We only used complete grain
299 trajectories showing several hops, but discarded incomplete trajectories, photos with unclear
300 grain detection from the black-white conversion, and photos comprising several grains. For the
301 top camera, we only calculated the lateral and downslope (X, Y) coordinates of the trajectories,
302 as we could not detect the actual impact positions.

303 We surveyed the evolving foam bed topography approximately every one to two hours
304 in each experiment. During this time, we stopped the particle feed and removed any
305 accumulated foam dust using compressed air. The foam surface was surveyed from two
306 positions above the flume using a terrestrial laser scanner, TLS (FARO FOCUS 3D), which
307 delivered 3D pointclouds (i.e., X, Y, Z -coordinates) with a mean spatial resolution of ~ 1 mm.
308 The individual, subsequent TLS-measured pointclouds were co-registered on the initial smooth
309 surface using twelve fixed target points along the flume walls (0.1m-diameter wooden spheres,
310 which allowed for calculating their centers; Figure 2B and 2C). Vertically differencing the co-
311 registered pointclouds using the M3C2 algorithm in cloudcompare software (CloudCompare,
312 2022; Lague et al., 2013), we calculated transient spatial foam abrasion and also noted the total
313 abrasion volume (i.e., total abrasion amount over the whole flume surface; V_{flume} [m^3]).

314

315 3.2 Fixed-Bed Experiments

316 The fixed-bed experiments (*FB*) were designed to gain more data on grain hop
 317 trajectories but using a simpler setup than the erodible-bed experiments. The experiments used
 318 a tilting chute that was 1.1 m long and 0.1 m wide. Six experiments were conducted (*FB1-FB6*),
 319 each with identical parameters except that the flume bed slope, θ_{slope} , was varied between 20°
 320 and 45° (Table 1; lower part). The experiments used the same rounded andesite gravel as
 321 experiments *EB3* and *EB4*. The flume bed consisted of the same foam as in the erodible-bed
 322 experiments, but since it was only traversed by a hundred grains over time, abrasion was
 323 negligible, and the topography remained planar. Grains were fed into the chute individually by
 324 hand. A high-speed lateral-view camera (the same as described above) was used to capture
 325 grain trajectories, and grain trajectory analysis was the same as in the erodible bed
 326 experiments.

327

328 3.3. Comparing the Model to Experiments and Natural Cases

329 As we want to verify the dry rockfall abrasion theory to represent a feasible hillslope
 330 erosion process, we (i) calibrate the DGAM model to reproduce the experimental observations
 331 of the *EB* and *FB*, then (ii) explore grain trajectories and abrasion varying hillslope angle and
 332 rockfall grain size, and finally (iii) scale the model to predict natural hillslope topography.

333 To run the model for the experimental setups, grain reflection from the flume walls was
 334 accounted for by stopping a grain's trajectory on the last cell in front of the wall. From there, it
 335 starts a new trajectory with its given variables but in a new direction ξ . Mean foam abrasion
 336 per grain impact, V_{cell} [m³], for an experiment of a given flume slope and grain type (Table 1)
 337 was calculated as:

338

$$339 \quad V_{cell} = \frac{V_{flume}}{n_{grains,tot} n_{imp,tot}} = \frac{V_{flume} m_{grain} l_{hop}}{m_{grains,tot} l_{flume}} \quad (11)$$

340

341 by estimation of the number of grains used, $n_{grains,tot}$ [-] (i.e., the total sediment mass fed into
 342 the experiment, $m_{grains,tot}$ [kg], divided by a single grain's mass, m_{grain}), and the mean
 343 number of impacts per grain along the flume, $n_{imps,tot}$ [-] (i.e., flume length, l_{flume} [m], divided
 344 by mean grain hop length, l_{hop}). To convert the experimental results into the grid world of the
 345 DGAM model, we assumed this abrasion volume is equally distributed over a model cell that is
 346 impacted by a grain (i.e. $V_{cell} = w_{cell} d_{cell}^2$, with $d_{cell} = d_{grain}$, as defined above). This
 347 assumption is reasonable, given the observation of generally platelet-shaped bedrock
 348 fragments abraded from grain impacts (Beer and Lamb, 2021). We then scaled the grain
 349 erosivity factor, k_{ero} , as the fraction between V_{cell} and the surface-normal component of the
 350 grain's mean kinetic impact energy, $\varepsilon_{kin,n}$ (Equation 9).

351 Using the calculated k_{ero} values and the measured initial grain entrance variables
 352 ($v_{out,0}$, $\alpha_{out,0}$ and $l_{hop,0}$) for each erodible-bed experiment *EB* (Table 1, upper part), we
 353 iteratively fit the DGA model (mode I, i.e. pure grain hopping) shock term coefficient, κ_{shock} , to

354 best reproduce the means of the observed grain trajectory variables and foam surface abrasion
355 rates of the experiments.

356 Having calibrated the model, we used it to explore the rockfall transport and impact
357 abrasion over a range of natural hillslope angles ($5 < \theta_{slope} < 45$) and grain sizes ($0.1\text{m} < d_{grain}$
358 $< 1\text{m}$). To model dry rockfall abrasion on rocky hillslopes under natural scenarios of hillslope
359 angle, grain sizes and lithology, we scaled the bedrock abrasion rate (V_{cell}) according to the
360 rock tensile strength following

$$361 \quad V_{rock} = V_{cell} \left(\frac{\sigma_{foam}}{\sigma_{rock}} \right)^2 \quad (12)$$

363 where V_{rock} [m^3] is the volumetric abrasion for any bedrock cell of tensile strength σ_{rock} (Beer
364 and Lamb, 2021; Scheingross et al., 2014).
365
366

367 4. Results

368 4.1 Topographic evolution in the experiments

369 All five erodible-bed experiments (*EB*; Table 1, upper part) evolved in a similar pattern,
370 and the final bed topographies resembled each other (Figure 3B). Here, we describe the general
371 evolution of these experiments to document the dry abrasion process, using *EB5* as an example
372 (Figure 3A). Grains discretely hopped down the foam surface and abraded it by incremental
373 impact abrasion, resulting in tiny pit craters and abraded foam dust creating lasting topography
374 (cf. Figure 1H). Initial grain abrasion pits down the entrance transiently grew into larger hollows
375 from ongoing impacts of subsequent grains (Figure 3A, left panel, shown for *EB5*), although
376 separate hollows were less distinct for the largest grains used in *EB1*. Grains leaving these
377 hollows initiated faint (mm-deep), parallel rills down the slope. Reaching a depth of around one
378 grain diameter, these hollows laterally coalesced into a trough, and the rills further evolved
379 (Figure 3A, central panel). This process is portrayed by the temporal evolution of the lateral
380 profiles through the hillslope (Figure 4A, upper panel). Over time, the rills extended in depth
381 and converged downslope into a central main channel (Figure 3A, right panel; Figure 4A, lower
382 panel). This channel's long profile maintained a slight bumpiness over time (Figure 4D), arising
383 from the subsequent evolution of new troughs, whose rims transiently traversed downslope
384 (Figure 3A, right panel). This pattern emerged in all erodible bed experiments (Figure 3B).

385 Throughout the experiments, some grains came to rest, though they were soon hit by
386 mobile grains and remobilized. So, permanent spatial cover generally did not occur on the main
387 foam board, even at the lowest experimental slope of $\theta_{slope} = 17^\circ$ (*EB1*; Table 1). However,
388 when a topographic depression (as the upper trough) reached a depth of two grain sizes
389 relative to its downslope rim, it gradually got clogged by resting grains, which formed a
390 stationary cover in the depression. Subsequent grains laterally traversed this patch of grains
391 and funneled into the evolving main central channel, uniting the former rills downslope
392 (Figure 3A, right panel); a similar sequence was described for *EB1* by Sun et al. (2021). Due to
393 the focusing of the grains into the central trough, lateral parts of the foam surface experienced

394 a decreasing number of grain impacts over time (Figure 4B), and they gradually abraded slower
 395 (Figure 4C; shown here is vertical abrasion equivalent to w_{cell} , for comparison). This
 396 morphodynamic feedback resulted in a channelized hillslope for all erodible-bed experiments,
 397 independent of hillslope angle or grain size (Figure 3B). The current pattern of the abrasion
 398 measurements therein reflected the current surface topography, e.g., the eroded rills (Figure
 399 4C upper panel vs. Figure 3A central panel).

400 When the patch of static grains in the upper trough initiated, it grew laterally and in
 401 height due to the higher pocket friction angle of the grain patch relative to the foam board (cf.
 402 Table 1). Once this grain pile backed up onto the peg board, the experiment was terminated
 403 (Figure 2B). Without the upslope limitation of the experimental facility, the grains probably
 404 would have continued piling until reaching their pocket friction angle, resulting in a grain
 405 avalanche, followed by a subsequent pile-up, and so on. Final bedrock topographies typically
 406 consisted of an upslope trough filled with a static grain patch, with a channel that extended and
 407 became less defined downslope (Figure 3B and Figure 4D; shown after sediment cover patch
 408 removal).

409 Changing the grain inlet width for the erodible-bed experiments (flume-wide for *EB1*,
 410 *EB2*, and *EB5*, central for *EB3* and *EB4*; Table S2) dictated the lateral extend of the upper trough
 411 (Figure 3B). The larger the grain size of the experiment, the farther the trough extended
 412 downslope (cf. *EB1* vs. *EB5*). Regardless of inlet width or particle size, all experiments showed a
 413 smooth rim at the trough outlet, followed by rills and a subsequent emerging trough, which
 414 initiated a channel (Figure 3A and Figure 4D).

415

416 **4.2. Grain trajectories and model calibration**

417 On average, for the erodible-bed experiments *EB1-EB3* and *EB5* (for *EB4*, there were too
 418 few measurements available for robust statistics), grains hopped by $\bar{l}_{hop} = 0.19 \pm 0.11$ m at
 419 $\bar{h}_{hop} = 0.02 \pm 0.02$ m height (mean and standard deviation) (Figure 5, grey boxplots; Table S2).
 420 They impacted at angles of $14 \pm 14^\circ$ above the respective foam surface (i.e., $\bar{\alpha}_{in} - \theta_{slope}$).
 421 The grain's hop lengths, hop heights, and impact angles were insensitive to the hillslope angle.
 422 However, the mean impact velocities, $1 < \bar{v}_{in} < 2$ m/s, increased with steeper hillslope
 423 angles. Deflection angles and deflection velocities generally equaled their impact pendants, so
 424 little kinetic energy was lost by the impacts. Mean initial grain entrance velocity from the peg
 425 board was around $v_{in,0} = 1.1$ m/s in the erodible-bed experiments. In the fixed-bed
 426 experiments, these velocities were higher (~ 1.5 m/s), resulting in increased hop lengths, impact
 427 angles, and impact velocities (Figure 5, white boxplots).

428 Derived vertical grain impact abrasion volumes per cell area, w_{cell} (i.e. V_{cell} / d_{cell}^2 ; cf.
 429 Equation 11) in the order of μm decreased with increasing slope angle (Figure 6A). This pattern
 430 is consistent with impacting grain's grain erosivity, k_{ero} (i.e. $V_{cell} / \varepsilon_{in,z}$), with some uncertainty
 431 for smaller, rounded grains of low erosivity, while even smaller but angular grains maintained
 432 their erosivity even for low impact energies (*EB5*; Figure 6B; Table 1). Normalizing k_{ero} values
 433 by grain cross-sectional area or cell size, d_{grain}^2 , resulted in an erosivity measure that collapsed
 434 the data of the fixed-bed experiments with round grains (*FB1-FB4*) around 0.001, while for the

435 angular grains, it remained higher ($k_{ero}/d_{grain}^2 = 0.003\text{m/J}$; Figure 6C; Table 1). These values can
 436 be used to calculate the DGA model's k_{ero} factor for a given grain size.

437 To calibrate the model using the experiments, we set k_{ero} based on the observed
 438 erosion amounts (Figure 6B). Next, we kept the observed initial grain entrance variables ($v_{in,0}$,
 439 $\alpha_{out,0}$ and $l_{hop,0}$) fixed in the model and varied the shock term coefficient, κ_{shock} , to best
 440 reproduce the suite of the mean trajectory parameters for each erodible-bed and fixed-bed
 441 experiment. Comparing the predicted versus the modeled means of the grain trajectory
 442 parameters l_{hop} , $v_{in,z}$, α_{in} , and V_{cell} (the latter parameter only for the erodible-bed
 443 experiments), we identified experiment-specific κ_{shock} values with the first closest general
 444 agreement (Figure 7 for EB2; cf. Figure S1 for all experiments). All these identified values fell in
 445 a narrow range around $\kappa_{shock} = 0.8 \text{ m}^{-1}$.

446

447 4.3. Model and experimental comparison

448 Predictions from the κ_{shock} -calibrated model generally fit the pattern of the measured
 449 PIV-derived trajectory parameters along the flume, though the range of the predictions was
 450 much lower (mean deviation -15% and range -60% for EB2 in Figure 8). The largest deviations
 451 existed for the predicted grain hop length, l_{hop} (-65%, Figure 8A), and the deflection velocities
 452 (-15%, Figure 8D), both mainly further downslope of the flume. Both grain impact and
 453 deflection angles were overpredicted at the flume's entrance. The impact angle, α_{in} , soon
 454 matched the observations, but the deflection angle, α_{out} , remained increased (6%, Figure 8E-F).
 455 Overall the grain impact velocities were met (-5% deviation, Figure 8B, C) and thus also the
 456 initially relatively increased impact abrasion fit the calculated values along the flume (-5%,
 457 Figure 8G).

458 All grain trajectory parameters for a fixed grain size increased with a steeper hillslope
 459 angle (Figure 9A; for $d_{grain} = 0.03\text{m}$). Over the range of $\theta_{slope} = 20^\circ$ to 45° hop length and
 460 impact velocity doubled, while impact angles remained more constant relative to the surface
 461 slope (Figure 9A; upper three panels). The resulting abrasion volume remained within one order
 462 of magnitude for volumetric impact abrasion, V_{cell} , and also for local erosivity (i.e., abrasion per
 463 meter downslope, V_{cell} / l_{hop} ; Figure 9, two lower panels). DGAM-predictions over $\theta_{slope} =$
 464 5° to 45° for both round grains ($d_{grain} = 0.03\text{m}$, representative for EB3, EB4, and FB1-FB6) and
 465 for angular grains (EB5) followed the general trends, in which angular grains consistently
 466 underpredicted observed abrasion volume (V_{cell} ; Figure 9A, two lower panels).

467 In contrast to the influence of slope angle, grain trajectory parameters showed more
 468 sensitivity to increasing grain size when holding slope fixed (Figure 9B; for $\theta_{slope} = 35^\circ$). Over
 469 the range of $d_{grain} = 0.015$ to 0.036m hop length, impact velocity, and impact angle all
 470 doubled (upper three panels of Figure 9B). Grain impact abrasion and local erosivity increased
 471 nonlinearly with grain size following a strong trend (two lower panels of Figure 9B; impact
 472 abrasion was not measured for FB4, but the predicted value from the measured impact
 473 energies was comparable to EB5). Accordingly, and from a general perspective of natural
 474 hillslopes, rocky surfaces with slope angles ranging from $\theta_{slope} = 15^\circ$ to 45° and impacted by
 475 rockfall grains of $d_{grain} = 0.01\text{m}$ to 1.00m diameter may experience local impact abrasion

476 volumes spanning six orders of magnitude (Figure S2; calculated using the erosivity for angular
 477 grains, as in *EB5*; Figure 6B, C). Herein, the influence of slope angle is inferior as compared to
 478 grain size. The abrasion volumes predicted for laboratory foam can be scaled to abrasion
 479 volumes of any (massive) bedrock by the inverse square of the material's tensile strengths
 480 (Equation 13).

481

482 **4.4 Model exploration**

483 Having calibrated the model, we sought to explore the impact of the upstream
 484 boundary condition on bedrock landforms developed by rockfall. For this, we simulated
 485 topography evolution from an initially smooth, sloping plain, similar to the experiments, with
 486 rockfall fed in from the top of the domain. We set the DGAM parameters to be more realistic
 487 for natural cases, including larger, angular rockfall grains ($m_{grains,tot} = 800\text{tons}$ of $d_{grain} =$
 488 0.20m) on a steep granite hillslope ($\theta_{slope} = 35^\circ$; $\sigma_{rock} = 5\text{MPa}$, cf. Equation 12; $k_{ero} =$
 489 0.003m/J , cf. Figure 6C, C; $\kappa_{shock} = 0.8\text{m}^{-1}$, cf. Figure 7). All other parameters were set as in *EB2*
 490 (Φ_{surf} , grain density, $v_{out,0}$, $\alpha_{out,0}$ and $l_{hop,0}$). We conducted two numerical experiments with
 491 all parameters equal except for a change in the feed of rockfall: Uniform feed over the center of
 492 the model domain (cross-sections in Figure 10A, long profile in Figure 10C) vs. rockfall dispersed
 493 over three source areas (Figure 10B and D).

494 For the case of a uniform central rockfall entrance, the initially planar hillslope surface
 495 developed a deepening trough at the entrance, which sourced into a channel with decreasing
 496 depth further downslope (panels of Figure 10A; more panels in Figure S3A). This process was
 497 driven by steering of grains into the channel center, increasing abrasion there (transient lateral
 498 grain distribution in the third panel of Figure 10A; cf. grain trajectories and local impact
 499 abrasion in Figure S3C and E). Down the hillslope, the hopping grains produced a sequence of
 500 intermittent and downslope-wandering concave troughs and convex rims of decreasing size,
 501 comparable to the topographic slope evolution during the experiments (Figure 10C vs. Figure
 502 4D). The experiment ended when the upper trough reached a depth of one grain diameter
 503 relative to its downslope rim, capturing all subsequent grains.

504 Modeling with the same number of grains as before, but fed onto the hillslope in three
 505 separated inlets (Figure 10B; more cross-sections shown in Figure S3B), resulted in comparable,
 506 but smaller concave-shaped channels downslope, i.e., in parallel rills that started coalescing.
 507 This experiment also stopped due to over-deepening of the upper trough (Figure 10D), after a
 508 remaining wider lateral grain distribution and abrasion than in the other experiment
 509 (Figure 10B third panel; Figure S3D and F).

510

511 **5 Discussion**

512 **5.1 Model calibration and validation**

513 It is currently not possible to compare our model predictions to natural erosion rates
 514 because the model requires specification of rockfall frequency, rock size and bedrock strength,
 515 which are generally unknown. Ultimately, a complete model of landscape evolution by dry
 516 rockfall will need to incorporate these rockfall generation processes, which can then be coupled

517 to model rockfall abrasion. Due to the lack of field constraints, we turned to scaled laboratory
 518 experiments to test the model. By varying hillslope angle, grain size, and grain shape, we
 519 calibrated a cellular, dry grain trajectory abrasion model by means of grain shape erosivity and
 520 an impact shock term, κ_{shock} (DGAM; Figures 2, 6 and 7). The grain trajectory velocities, angles,
 521 and hop length only varied within their magnitude in our *EB* flume experiments and they
 522 showed a larger spread for the *FB* due to a small test population of some tens of grains (Table 1
 523 and Table S2; Figure 5 and Figure 8). The calibrated model did not entirely reproduce these
 524 measured grain trajectories (fewest the hop length; Figure 8), which may be attributable to the
 525 larger range of the experimental trajectory variables due to uneven grain shape (Figure 5).
 526 Varying the impact shock term, κ_{shock} , could account for this discrepancy by generating a wider
 527 distribution of trajectories. Grain shape likely has a nonlinear influence both on grain mobility
 528 (angular grains have large pocket and surface friction angles; Table 1; Figure 9) and on grain
 529 impact erosivity (angular grains will be more erosive; Neilson and Gilchrist, 1968). Though,
 530 summed impacts of a given grain shape mixture may cancel out varying abrasion volumes of
 531 different grain shapes, as indicated by the general collapse of experimental abrasion data for
 532 local impact abrasion (Figure S4D-F). This leveraging is also reflected in the deviation of model-
 533 predicted lower deflection velocities but higher deflection angles that still led to acceptable
 534 abrasion rates based on a fixed shock term (Figure 8D, F, and G).

535

536

5.2 Effect of slope and grain size

537 Constraining grain impact abrasion volume is a crucial factor in the process, and grain
 538 size showed to be of dominant influence compared with hillslope angle (Figure S2). Modelled
 539 trajectory parameters increased modestly with increasing slope angle, and abrasion volume
 540 only rose by one order of magnitude from shallow to steep slopes (Figure 9A). All parameters
 541 also increased with larger grain size (Figure 9B). Importantly, grain impact erosivity nonlinearly
 542 rose, spanning six orders of magnitude from pebbles to 1m boulders (Figure 9B lower panels
 543 and Figure S2) due to the nonlinear impact energy-dependence on grain diameter cubed (cf.

544 $m_{grain} = \sigma_{rock} \frac{4}{3} \pi \left(\frac{d_{grain}}{2} \right)^3$). This matches the high erosivity of large (meter-sized) rockfall
 545 boulders analyzed in rockfall runout studies (Bickel et al., 2020a, 2020b; Volkwein et al., 2011)
 546 and in previous abrasion experiments (Mokudai et al., 2011), and matches their importance in
 547 fluvial abrasion (Beer and Lamb, 2021; Turowski et al., 2015).

548 Within a distribution of rockfall grain sizes, the largest grains will have an immediate
 549 effect on surface morphology since both subsequent grain trajectories will be more influenced
 550 by their erosive impact on surface roughness, and their momentum-dependent runout distance
 551 is the largest (Kokelaar et al., 2017). Though, the actual/transient grain size distribution will
 552 determine the representative grain size that may be applicable for average modeling. Field data
 553 on individual (caprock) rockfall grain size distributions are lacking to our knowledge, though it
 554 could, e.g., be derived from rocky hillslope's fracture-spacing (Neely and DiBiase, 2020) and
 555 then allow assessment of the interplay between rockfall erosivity and slope erodibility.

556

5.3 Effect of substrate strength

557 As grain impact erosivity depends on the surface-normal component of kinetic impact
 558 energy, independent of the actual medium through which the grain moves (e.g., air or water), it
 559 scales inversely with bedrock substrate tensile strength, σ_{rock} (Beer and Lamb, 2021;
 560 Scheingross et al., 2014). Thus, dry grain impact abrasion, $V_{cell} = k_{ero} \varepsilon_{kin,n}$, can be
 561 transformed to fit into the bedrock erodibility framework established for fluvial abrasion and
 562 grain drop experiments on rocks of different strengths, $V_{rock} = c_{ero} \frac{\varepsilon_{kin,n}}{\sigma_{rock}^2}$ (with a bedrock
 563 erodibility conversion factor of $c_{ero} = 3.8 \times 10^4 \text{ J/Pa}^2$; Beer and Lamb, 2021). Conversely, any
 564 massive bedrock as defined by its tensile strength can be applied within DGAM by multiplying
 565 grain impact erosivity (Equation 12). Compared to our used foam substrate, V_{rock} would shift to
 566 one order of magnitude higher abrasion rates for a weak sandstone ($\sigma_{rock} = 0.1 \text{ MPa}$) or to
 567 four orders of magnitude lower abrasion rates for quartzite ($\sigma_{rock} = 20 \text{ MPa}$; cf. the measured
 568 rock tensile strengths in Sklar and Dietrich, 2001).

569 There may be additional important tradeoffs between the erodibility of bedrock and the
 570 frequency and magnitude of rockfall events. For example, bedrock tends to be stronger in
 571 massive rock with low fracture density, like granite (cf. Figure 1E), which should slow rockfall
 572 erosion rates by reducing k_{ero} . In addition, granite also tends to weather into small grains,
 573 which would have low kinetic energy and therefore could reduce rockfall erosion rates further
 574 (Equation 9). In contrast, jointed rocks like sandstone or columnar basalt produce more intact
 575 rock blocks (cf. Figure 1A and B; Ward et al., 2011). Due to the more-than-linear dependence of
 576 abrasion on impactor size (Figure 9B, lower panels), fewer more massive rocks would produce
 577 more erosion than more frequent events with smaller rocks. These ideas could be incorporated
 578 in a future effort to describe the rockfall generation process, which is needed to drive the
 579 rockfall abrasion model.

580 **5.4. Rockfall erosion on low gradients**

581 Our experiments and modelling confirm that bedrock hillslopes can be eroded by dry
 582 rockfall abrasion even below the angle of repose (Figure 3; DiBiase et al., 2017; Pelletier et al.,
 583 2008; Sun et al., 2021). Given energetic rockfall and low friction angles relative to the surface
 584 roughness (DiBiase et al., 2017), even small grain sizes are able to traverse rocky slopes (Figure
 585 9B). As their impact energy is not diffused into granular debris like on granular substrate (Figure
 586 1G), it contributes to rock fracturing and subsequent abrasion (Figure 1H). Thus, dry rockfall, as
 587 an endmember of dry granular avalanching (Howard, 1998), is an erosive process not restricted
 588 to steep alpine environments.

589 The abundance of rockfall on rocky slopes in both dry and humid areas permit to
 590 elucidate the absolute and relative contribution of rockfall-driven erosion to earthen and
 591 planetary surface evolution, so far generally ascribed to fluvial or aeolian erosion (e.g., Figure
 592 1A to D). While in steeper areas rockfall may outpace other erosive processes and create
 593 indicative topographic features (cf. Howard and Selby, 2009), at the foot slopes of lower
 594 gradient, dry bedrock abrasion could set preferential routes for fluvial mass transport processes
 595 and this way enhance their channelization.

596 **5.5. Formation of rocky chutes**

597 As shown, rockfall-prone hillslopes evolve into bumpy and channelized chute
598 topography (Figure 3 and Figure 4A and D; Blackwelder, 1942), which steers grains into
599 preferential pathways resulting in topographic feedback (Figure 4B and C; cf. Sun et al., 2021).
600 This transient process was successfully reproduced by the dry grain abrasion model DGAM
601 fitted with a fixed impact shock term coefficient, $\kappa_{shock} = 0.8 \text{ m}^{-1}$ (Figure 10 and Figure S3).
602 Improvement of this calibration could have been reached by better constraining the initial grain
603 entrance conditions, though we took the approach of modeling the inlet conditions as random.
604 The experimentally observed and modeled topographies generally resemble earthen and
605 planetary rocky hillslope topography (Blackwelder, 1942), showing bedrock chutes and gully
606 alcoves with downslope bumps and channels (Figure 3 and Figure 10 vs. Figure 1A to D). The
607 lateral grain mobility (so far treated by probabilistic direction-sampling in DGAM, Table S1) was
608 not retrievable from the vertical PIV camera in our experiments. Grain spread transience would
609 help quantify the topographic steering feedback and its separation from diffusional processes
610 (Jop et al., 2005; Williams and Furbish, 2021).

611 As long as rocky hillslopes remain free of cover (from regolith, saprolite, or vegetation),
612 continuous and local dry grain abrasion will create rills that fuel a sequence of downhill-
613 wandering troughs and rims (Figure 3B and 10A, B; Sun et al., 2021; cf. examples in Figure 1F
614 and H), somehow an antipode to upstream-migrating knickpoints in (bedrock) rivers driven by
615 fluvial sediment transport (Berlin and Anderson, 2007; Crosby and Whipple, 2006; DiBiase et al.,
616 2015; Grimaud et al., 2016). Grain routing around sediment patches (Figures 1A and 3B) and
617 grain deflection from elevated topography will enhance downhill channelization, which over
618 time can lead to chutes (Figure 3A right panel, Figure 4C) or even gully channels (Figure 1D) by a
619 self-enhancing process. Model-predicted topographies resembled both throughs (Figure 10A vs.
620 Figure 3A right panel) and parallel rills (Figure 10B vs. Figure 3A central panel). The physical
621 steering process of grains around resting sediment patches, as in the troughs of the
622 experiments (Figure 3B), has not implicitly been implemented in the DGA model so far, and
623 would require parameterizations of grain-grain interaction, grain piling (with varying angle of
624 repose), and release mechanisms.

625 Talus cover from lower-sloping regions downhill reaching up onto the active abrasion
626 area will suddenly terminate the process and seal the rocky surface due to rockfall grains
627 starting to rest below their angle of repose, i.e., shielding a so-called sub-debris or Richter
628 denudation slope below (a rectilinear, 35.0° thinly-covered rocky hillslope; Rapp, 1960).
629 Termination will happen given short hillslope lengths, large amounts of simultaneous rockfall
630 grains (i.e. dry grain avalanches), or low talus removal rates by other processes. Thus, there is
631 potential that large talus cones or ramparts actually cover and hide channelized rocky slopes
632 initially created by dry rockfall abrasion – a topic that could be verified by studying impact
633 crater degeneration or escarpment retreat in dry planetary areas (Golombek et al., 2014; Ward
634 et al., 2011).

635 **5.5. Application to other planets**

636 Dry grain abrasion modeling can generally be performed for any planetary body by
637 adjusting gravitational acceleration. Though, there likely is no significant influence of this
638 parameter on model mode II (grain rolling and sliding; not studied here; cf. Atwood-Stone and

639 McEwen, 2013), as there also is none on mode I (grain hopping) besides the influence on the
640 acceleration of the grains during hopping. Air (or other gas) drag during the grain trajectories is
641 neglected in the model since we deal with relatively low velocities and small, compact grains.
642 Specifically, dry grain abrasion could be modeled in concert with other erosion processes (such
643 as diffusion) to study the degradation of planetary crater walls, etc. (Golombek et al., 2014).
644 This will help verify if dry bedrock abrasion is a reason why crater walls remain rocky or how
645 low-sloping sinuous gully channels are maintained over time (Mangold et al., 2010).

646 Dry grain abrasion modeling on planetary surfaces is feasible considering rock or ice-
647 cemented sediments using estimates of the substrate's tensile strengths (Beer et al., 2019). For
648 example, low-fractured basaltic rock on Mars may have a tensile strength of $\sigma_{rock} \sim 10$ MPa,
649 which certainly is much lower at fractured impact craters (Wright et al., 2022; Figure 1D). Ice-
650 cemented sediment near the melting point has tensile strengths similar to our applied foam
651 ($\sigma_{foam} = 0.1$ MPa), whereas colder permafrost can have tensile strengths again similar to basalt
652 (Akagawa and Nishisato, 2009; Azmatch et al., 2010; Yuanlin and Carbee, 1987). Given dry
653 regions on Earth, absolute dryness on the Moon, and current dry conditions on Mars (Figure 1A
654 to D), together with abundant rocky hillslope areas and rockfall activity (Bickel et al., 2020a,
655 2020b; Dickson and Head, 2009; Kumar et al., 2013; Vijayan et al., 2022; Xiao et al., 2013), the
656 rockfall abrasion process has potential to be a local to regional sculptor of planetary hillslopes.
657 Shattered rocky crater walls and caprock-topped badlands are ideal sites for the process to
658 occur. The spatio-temporal imprint of dry rockfall abrasion, specifically its distinction from and
659 interaction with fluvial processes (Figure 1G vs. H; Levin et al., 2022), remains to be studied in
660 detail, both for Earth and planetary hillslopes.

661

662 **5 Conclusions**

663 Our experiments and modeling show that bedrock abrasion by dry, impacting rockfall can
664 erode and in some cases channelize rocky hillslopes. The model captures the trends in the
665 experiments to first order by including the physics of ballistic trajectories and a bedrock wear
666 (abrasion) relation that depends on the surface-normal kinetic energy of the impactor. Erosive
667 grains can hop on slopes even shallower than the angle of repose (at least down to 20°), and
668 thus contribute to landscape evolution in areas where fluvial and debris flow processes are
669 thought to dominate. We found that increasing rockfall grain size has the most substantial
670 effect to increase abrasion amounts due to a nonlinear relationship. Increasing hillslope
671 gradient also caused faster erosion rates.

672 Hopping grains are routed around topographic highs, which steer grains trajectories in a
673 self-enhancing feedback. First, a bumpy surface evolves with patches of immobile sediment
674 collecting in lows (troughs) due to greater friction angles of grain piles. Around these piles and
675 bedrock highs, shallow rills form, which coalesce into chutes and finally into emerging channels
676 further downslope. These channels increasingly attract subsequent grains, focusing abrasion
677 into their centers, and cause a sequence of troughs wandering downslope. The rockfall abrasion

678 process will terminate abruptly, where talus grows uphill from the toe of the hillslope or by
679 coalescence of local resting sediment patches.

680 Given abundant rocky hillslopes and rockfall sources from cliffs and outcrops (Blackwelder,
681 1942; Howard and Selby, 2009; Ward et al., 2011), dry impact-driven bedrock abrasion is a
682 conceivable contributor to Earth and planetary hillslope evolution. It could be important in high
683 mountain rockfall areas, dry climate scarpland retreat, and in planetary surface crater decay.
684 The model explicitly includes gravity and can be scaled to other planets.

685

686 **Acknowledgments, Samples, and Data**

687 We are thankful to Joel Scheingross for help with PU foam selection, to Roman DiBiase
688 for providing his model code, and to Kim Miller for measuring grain friction angles. Thorough
689 comments from three anonymous reviewers and the associate editor Kathy Barnhart greatly
690 helped to improve the manuscript. This study was supported by SNSF grant P2EZP2_172109 to
691 ARB, Caltech SURF fellowships to JNF and ZM, China Scholarship Council grant 201906410043
692 and NSFC Grant 42202120 to ZS, and NASA grant 80NSSC19K1269 and NSF grant 1558479 to
693 MPL.

694

695 **Data Accessibility**

696 The experimental data and the dry gravel abrasion model DGAM code (in R language)
697 will be made publicly available at <https://data.caltech.edu> or at <https://fdat.uni-tuebingen.de/>.

698

699 **Notation**

| | | |
|-----|------------------|--|
| 700 | a_{grav} | acceleration due to gravity [m/s ²] |
| 701 | c_{ero} | bedrock erodibility conversion factor [J/P ²] |
| 702 | d_{cell} | model cell size [m] |
| 703 | d_{grain} | rockfall grain diameter [m] |
| 704 | h_{hop} | grain hop height (trajectory maximum above crossed cell boundaries) [m] |
| 705 | k_{ero} | bedrock erosion factor (grain erosivity) [m ³ /J or ms ² /kg] |
| 706 | l_{flume} | length of the laboratory flume [m] |
| 707 | l_{hop} | grain hop length [m] |
| 708 | $l_{hop,0}$ | grain hop length at entrance of a grain into the model domain [m] |
| 709 | m_{grain} | rockfall grain mass [kg] |
| 710 | $m_{grains,tot}$ | total mass of all grains in one experiment [kg] |
| 711 | n_{cells} | number of DEM cells traversed by a grain's trajectory [-] |
| 712 | $n_{grains,tot}$ | total number of grains used in an experiment [-] |
| 713 | $n_{imps,tot}$ | total number of grain impacts per grain down the laboratory flume [-] |
| 714 | t_{hop} | grain hop time [s] |
| 715 | V_{flume} | total volumetric foam abrasion of an experiment from grain impacts [m ³] |
| 716 | V_{cell} | volumetric abrasion of a cell by a grain impact [m ³] |
| 717 | V_{rock} | volumetric abrasion of a bedrock cell by a grain impact [m ³] |
| 718 | v_{in} | grain impact velocity [m/s] |
| 719 | $v_{in,0}$ | grain impact velocity at entrance of a grain into the model domain [m/s] |

| | | |
|-----|--------------------|--|
| 720 | $v_{in,n}$ | surface-normal component of the grain impact velocity [m/s] |
| 721 | v_{out} | grain deflection velocity [m/s] |
| 722 | $v_{out,0}$ | grain deflection velocity before entrance of a grain into the model domain [m/s] |
| 723 | w_{cell} | vertical cell abrasion or wear [m] |
| 724 | X, Y, Z | cell coordinate (X: downflume, Y: lateral, Z: vertical) [-] |
| 725 | $Z_{boundary}$ | surface height at the boundary between two DEM cells [m] |
| 726 | Z_{traj} | grain trajectory height above a cell boundary [m] |
| 727 | α_{in} | absolute grain impact angle [°] |
| 728 | $\alpha_{in,0}$ | absolute grain impact angle at entrance of a grain into the model domain [°] |
| 729 | α_{out} | absolute grain deflection angle [°] |
| 730 | $\alpha_{out,0}$ | absolute grain deflection angle at entrance of a grain into model domain [°] |
| 731 | ϵ_{kin} | grain kinetic impact energy [J] |
| 732 | $\epsilon_{kin,n}$ | surface-normal component of the grain kinetic impact energy [J] |
| 733 | Δt | grain impact time [s] |
| 734 | ΔXY | horizontal distance between two cells [m] |
| 735 | ΔZ | vertical distance between two cells [m] |
| 736 | ξ | grain hop direction in D8 [-] |
| 737 | κ_{shock} | impact shock term [1/m] |
| 738 | σ_{foam} | tensile strength of the polyurethane foam [MPa] |
| 739 | σ_{rock} | tensile strength of bedrock [MPa] |
| 740 | θ_{cell} | cell slope angle [°] |
| 741 | θ_{slope} | hillslope angle or flume slope angle [°] |
| 742 | Φ_{surf} | dynamic friction angle between grain and (bedrock) surface [°] |
| 743 | Φ_{pocket} | grain pocket friction angle [°] |
| 744 | μ_{eff} | effective grain friction angle [°] |

745

746 **References**

- 747 Akagawa, S., Nishisato, K., 2009. Tensile strength of frozen soil in the temperature range of the frozen fringe. *Cold*
748 *Reg. Sci. Technol.* 57, 13–22. <https://doi.org/10.1016/j.coldregions.2009.01.002>
- 749 André, M.-F., 1997. Holocene Rockwall Retreat in Svalbard: A Triple-Rate Evolution. *Earth Surf. Process. Landf.*
750 22, 423–440.
- 751 Atwood-Stone, C., McEwen, A.S., 2013. Avalanche slope angles in low-gravity environments from active Martian
752 sand dunes. *Geophys. Res. Lett.* 40, 2929–2934. <https://doi.org/10.1002/grl.50586>
- 753 Azmatch, T.F., Segó, D.C., Arenson, L.U., Biggar, K.W., 2010. Tensile Strength of Frozen Soils Using Four-Point
754 Bending Test 8.
- 755 Beer, A.R., Lamb, M.P., 2021. Abrasion regimes in fluvial bedrock incision. *Geology* 49, 682–686.
756 <https://doi.org/10.1130/G48466.1>
- 757 Beer, A.R., Lamb, M.P., Ulizio, T.P., Ma, Z., Hughes, M.N., Fraeman, A.A., Arvidson, R.E., Golombek, M.P.,
758 Dickson, J.L., 2019. Bedrock gully formation by dry rockfall, in: LPI Contrib. Presented at the Ninth
759 International Conference on Mars 2019.
- 760 Beer, A.R., Turowski, J.M., 2021. From process to centuries: Upscaling field-calibrated models of fluvial bedrock
761 erosion. *Geophys. Res. Lett.* <https://doi.org/10.1029/2021GL093415>
- 762 Benjamin, J., Rosser, N.J., Brain, M.J., 2020. Emergent characteristics of rockfall inventories captured at a regional
763 scale. *Earth Surf. Process. Landf.* 45, 2773–2787. <https://doi.org/10.1002/esp.4929>
- 764 Berlin, M.M., Anderson, R.S., 2007. Modeling of knickpoint retreat on the Roan Plateau, western Colorado. *J.*
765 *Geophys. Res.* 112, F03S06. <https://doi.org/10.1029/2006JF000553>
- 766 Bickel, V.T., Aaron, J., Manconi, A., Loew, S., Mall, U., 2020a. Impacts drive lunar rockfalls over billions of years.
767 *Nat. Commun.* 11, 2862. <https://doi.org/10.1038/s41467-020-16653-3>
- 768 Bickel, V.T., Conway, S.J., Tesson, P.-A., Manconi, A., Loew, S., Mall, U., 2020b. Deep Learning-Driven
769 Detection and Mapping of Rockfalls on Mars. *IEEE J. Sel. Top. Appl. Earth Obs. Remote Sens.* 13, 2831–
770 2841. <https://doi.org/10.1109/JSTARS.2020.2991588>
- 771 Blackwelder, E., 1942. The process of mountain sculpture by rolling debris. *J. Geomorphol.* 4, 324–328.
- 772 Brian Dade, W., Huppert, H.E., 1998. Long-runout rockfalls. *Geology* 26, 803. [https://doi.org/10.1130/0091-7613\(1998\)026<0803:LRR>2.3.CO;2](https://doi.org/10.1130/0091-7613(1998)026<0803:LRR>2.3.CO;2)

- 774 CloudCompare, 2022. CloudCompare (version 2.12) [GPL software].
775 Collins, B.D., Stock, G.M., 2016. Rockfall triggering by cyclic thermal stressing of exfoliation fractures. *Nat.*
776 *Geosci.* 9, 395–400. <https://doi.org/10.1038/ngeo2686>
777 Conway, S.J., Balme, M.R., Kreslavsky, M.A., Murray, J.B., Towner, M.C., 2015. The comparison of topographic
778 long profiles of gullies on Earth to gullies on Mars: A signal of water on Mars. *Icarus* 253, 189–204.
779 <https://doi.org/10.1016/j.icarus.2015.03.009>
780 Crosby, B.T., Whipple, K.X., 2006. Knickpoint initiation and distribution within fluvial networks: 236 waterfalls in
781 the Waipaoa River, North Island, New Zealand. *Geomorphology* 82, 16–38.
782 <https://doi.org/10.1016/j.geomorph.2005.08.023>
783 D’Amato, J., Hantz, D., Guerin, A., Jaboyedoff, M., Baillet, L., Mariscal, A., 2016. Influence of meteorological
784 factors on rockfall occurrence in a middle mountain limestone cliff. *Nat. Hazards Earth Syst. Sci.* 16, 719–
785 735. <https://doi.org/10.5194/nhess-16-719-2016>
786 Delannay, R., Valance, A., Mangeney, A., Roche, O., Richard, P., 2017. Granular and particle-laden flows: from
787 laboratory experiments to field observations. *J. Phys. Appl. Phys.* 50, 053001.
788 <https://doi.org/10.1088/1361-6463/50/5/053001>
789 DiBiase, R.A., Lamb, M.P., Ganti, V., Booth, A.M., 2017. Slope, grain size, and roughness controls on dry sediment
790 transport and storage on steep hillslopes. *J. Geophys. Res. Earth Surf.* 122, 941–960.
791 <https://doi.org/10.1002/2016JF003970>
792 DiBiase, R.A., Whipple, K.X., Lamb, M.P., Heimsath, A.M., 2015. The role of waterfalls and knickzones in
793 controlling the style and pace of landscape adjustment in the western San Gabriel Mountains, California.
794 *Geol. Soc. Am. Bull.* 127, 539–559. <https://doi.org/10.1130/B31113.1>
795 Dickson, J.L., Head, J.W., 2009. The formation and evolution of youthful gullies on Mars: Gullies as the late-stage
796 phase of Mars’ most recent ice age. *Icarus* 204, 63–86. <https://doi.org/10.1016/j.icarus.2009.06.018>
797 Dickson, J.L., Head, J.W., Kreslavsky, M., 2007. Martian gullies in the southern mid-latitudes of Mars: Evidence for
798 climate-controlled formation of young fluvial features based upon local and global topography. *Icarus* 188,
799 315–323. <https://doi.org/10.1016/j.icarus.2006.11.020>
800 Dorren, L.K.A., Maier, B., Putters, U.S., Seijmonsbergen, A.C., 2004. Combining field and modelling techniques to
801 assess rockfall dynamics on a protection forest hillslope in the European Alps. *Geomorphology* 57, 151–
802 167. [https://doi.org/10.1016/S0169-555X\(03\)00100-4](https://doi.org/10.1016/S0169-555X(03)00100-4)
803 Engel, P.A., 1978. *Impact Wear of Materials*. Elsevier.
804 Frayssines, M., Hantz, D., 2006. Failure mechanisms and triggering factors in calcareous cliffs of the Subalpine
805 Ranges (French Alps). *Eng. Geol.* 86, 256–270. <https://doi.org/10.1016/j.enggeo.2006.05.009>
806 Gabet, E.J., Mendoza, M.K., 2012. Particle transport over rough hillslope surfaces by dry ravel: Experiments and
807 simulations with implications for nonlocal sediment flux: PARTICLE TRANSPORT OVER ROUGH
808 SURFACES. *J. Geophys. Res. Earth Surf.* 117, n/a-n/a. <https://doi.org/10.1029/2011JF002229>
809 Golombek, M.P., Warner, N.H., Ganti, V., Lamb, M.P., Parker, T.J., Ferguson, R.L., Sullivan, R., 2014. Small crater
810 modification on Meridiani Planum and implications for erosion rates and climate change on Mars: Small
811 Crater Modification on Mars. *J. Geophys. Res. Planets* 119, 2522–2547.
812 <https://doi.org/10.1002/2014JE004658>
813 Grenon, M., Hadjigeorgiou, J., 2008. A design methodology for rock slopes susceptible to wedge failure using
814 fracture system modelling. *Eng. Geol.* 96, 78–93. <https://doi.org/10.1016/j.enggeo.2007.10.002>
815 Grimaud, J.-L., Paola, C., Voller, V., 2016. Experimental migration of knickpoints: influence of style of base-level
816 fall and bed lithology. *Earth Surf. Dyn.* 4, 11–23. <https://doi.org/10.5194/esurf-4-11-2016>
817 Guerin, A., Rossetti, J.-P., Hantz, D., Jaboyedoff, M., 2013. Estimating rock fall frequency in a limestone cliff using
818 LIDAR measurements 9.
819 Hales, T.C., Roering, J.J., 2007. Climatic controls on frost cracking and implications for the evolution of bedrock
820 landscapes. *J. Geophys. Res.* 112, F02033. <https://doi.org/10.1029/2006JF000616>
821 Heldmann, J.L., Mellon, M.T., 2004. Observations of martian gullies and constraints on potential formation
822 mechanisms. *Icarus* 168, 285–304. <https://doi.org/10.1016/j.icarus.2003.11.024>
823 Howard, A.D., 2007. Simulating the development of Martian highland landscapes through the interaction of impact
824 cratering, fluvial erosion, and variable hydrologic forcing. *Geomorphology* 91, 332–363.
825 <https://doi.org/10.1016/j.geomorph.2007.04.017>
826 Howard, A.D., 1998. Long profile development of bedrock channels, in: Tinkler, J., Wohl, E. (Eds.), *Geophysical*
827 *Monograph Series*. American Geophysical Union, Washington, D. C., pp. 297–319.
828 <https://doi.org/10.1029/GM107p0153>

- 829 Howard, A.D., Selby, M.J., 2009. Rock slopes, in: Parsons, A.J., Abrahams, A.D. (Eds.), *Geomorphology of Desert*
830 *Environments*. Springer Netherlands, Dordrecht. <https://doi.org/10.1007/978-1-4020-5719-9>
- 831 Jop, P., Forterre, Y., Pouliquen, O., 2005. Crucial role of sidewalls in granular surface flows: consequences for the
832 rheology. *J. Fluid Mech.* 541, 167. <https://doi.org/10.1017/S0022112005005987>
- 833 Kirkby, M.J., Statham, I., 1975. Surface Stone Movement and Scree Formation. *J. Geol.* 83, 349–362.
- 834 Kokelaar, B.P., Bahia, R.S., Joy, K.H., Viroulet, S., Gray, J.M.N.T., 2017. Granular avalanches on the Moon: Mass-
835 wasting conditions, processes, and features: Granular Avalanches on the Moon. *J. Geophys. Res. Planets*
836 122, 1893–1925. <https://doi.org/10.1002/2017JE005320>
- 837 Kumar, S.P., Keerthi, V., Senthil Kumar, A., Mustard, J., Gopala Krishna, B., Amitabh, Ostrach, L.R., Kring,
838 David.A., Kiran Kumar, A.S., Goswami, J.N., 2013. Gullies and landslides on the Moon: Evidence for dry-
839 granular flows: GULLIES AND LANDSLIDES ON THE MOON. *J. Geophys. Res. Planets* 118, 206–223.
840 <https://doi.org/10.1002/jgre.20043>
- 841 Lague, D., Brodu, N., Leroux, J., 2013. Accurate 3D comparison of complex topography with terrestrial laser
842 scanner: Application to the Rangitikei canyon (N-Z). *ISPRS J. Photogramm. Remote Sens.* 82, 10–26.
843 <https://doi.org/10.1016/j.isprsjprs.2013.04.009>
- 844 Lajeunesse, E., Mangeney-Castelnau, A., Vilotte, J.P., 2004. Spreading of a granular mass on a horizontal plane.
845 *Phys. Fluids* 16, 2371–2381. <https://doi.org/10.1063/1.1736611>
- 846 Lamb, M.P., Finnegan, N.J., Scheingross, J.S., Sklar, L.S., 2015. New insights into the mechanics of fluvial bedrock
847 erosion through flume experiments and theory. *Geomorphology* 244, 33–55.
848 <https://doi.org/10.1016/j.geomorph.2015.03.003>
- 849 Le Roy, G., Helmstetter, A., Amitrano, D., Guyoton, F., Le Roux-Mallouf, R., 2019. Seismic Analysis of the
850 Detachment and Impact Phases of a Rockfall and Application for Estimating Rockfall Volume and Free-
851 Fall Height. *J. Geophys. Res. Earth Surf.* 124, 2602–2622. <https://doi.org/10.1029/2019JF004999>
- 852 Leith, K., Moore, J.R., Amann, F., Loew, S., 2014. In situ stress control on microcrack generation and macroscopic
853 extensional fracture in exhuming bedrock. *J. Geophys. Res. Solid Earth* 119, 594–615.
854 <https://doi.org/10.1002/2012JB009801>
- 855 Levin, J.N., Dickson, J.L., Lamb, M.P., 2022. Evaluating the role of volatiles in bedrock chute formation on the
856 Moon and Mars. *Icarus* 373, 114774. <https://doi.org/10.1016/j.icarus.2021.114774>
- 857 Loye, A., Pedrazzini, A., Theule, J.I., Jaboyedoff, M., Liébault, F., Metzger, R., 2012. Influence of bedrock
858 structures on the spatial pattern of erosional landforms in small alpine catchments. *Earth Surf. Process.*
859 *Landf.* 37, 1407–1423. <https://doi.org/10.1002/esp.3285>
- 860 Mackey, B.H., Quigley, M.C., 2014. Strong proximal earthquakes revealed by cosmogenic ³He dating of prehistoric
861 rockfalls, Christchurch, New Zealand. *Geology* 42, 975–978. <https://doi.org/10.1130/G36149.1>
- 862 Mangold, N., Mangeney, A., Migeon, V., Ansan, V., Lucas, A., Baratoux, D., Bouchut, F., 2010. Sinuous gullies on
863 Mars: Frequency, distribution, and implications for flow properties. *J. Geophys. Res.* 115, E11001.
864 <https://doi.org/10.1029/2009JE003540>
- 865 Matasci, B., Stock, G.M., Jaboyedoff, M., Carrea, D., Collins, B.D., Guérin, A., Matasci, G., Ravanel, L., 2018.
866 Assessing rockfall susceptibility in steep and overhanging slopes using three-dimensional analysis of
867 failure mechanisms. *Landslides* 15, 859–878. <https://doi.org/10.1007/s10346-017-0911-y>
- 868 McDonald, R.R., Anderson, R.S., 1996. Constraints on Eolian Grain Flow Dynamics Through Laboratory
869 Experiments on Sand Slopes. *SEPM J. Sediment. Res. Vol.* 66. <https://doi.org/10.1306/D42683D3-2B26-11D7-8648000102C1865D>
- 870
- 871 Mergili, M., Jaboyedoff, M., Pullarello, J., Pudasaini, S.P., 2020. Back calculation of the 2017 Piz Cengalo–Bondo
872 landslide cascade with r.avaflow: what we can do and what we can learn. *Nat. Hazards Earth Syst. Sci.* 20,
873 505–520. <https://doi.org/10.5194/nhess-20-505-2020>
- 874 Messenzehl, K., Meyer, H., Otto, J.-C., Hoffmann, T., Dikau, R., 2017. Regional-scale controls on the spatial
875 activity of rockfalls (Turtmann Valley, Swiss Alps) — A multivariate modeling approach. *Geomorphology*
876 287, 29–45. <https://doi.org/10.1016/j.geomorph.2016.01.008>
- 877 Mokudai K., Ikeda H., Iijima H., Yuhora K., 2011. Experimental Study of Bedrock Erosion by Rock Fall. *Geogr.*
878 *Stud.* 86, 108–114. <https://doi.org/10.7886/hgs.86.108>
- 879 Montgomery, D.R., Dietrich, W.E., 1994. A physically based model for the topographic control on shallow
880 landsliding. *Water Resour. Res.* 30, 1153–1171. <https://doi.org/10.1029/93WR02979>
- 881 Moore, J.R., Sanders, J.W., Dietrich, W.E., Glaser, S.D., 2009. Influence of rock mass strength on the erosion rate of
882 alpine cliffs. *Earth Surf. Process. Landf.* 34, 1339–1352. <https://doi.org/10.1002/esp.1821>

- 883 Neely, A.B., DiBiase, R.A., 2020. Drainage Area, Bedrock Fracture Spacing, and Weathering Controls on
884 Landscape-Scale Patterns in Surface Sediment Grain Size. *J. Geophys. Res. Earth Surf.* 125.
885 <https://doi.org/10.1029/2020JF005560>
- 886 Neilson, J.H., Gilchrist, A., 1968. Erosion by a stream of solid particles. *Wear* 11, 111–122.
887 [https://doi.org/10.1016/0043-1648\(68\)90591-7](https://doi.org/10.1016/0043-1648(68)90591-7)
- 888 Pelletier, J.D., Kolb, K.J., McEwen, A.S., Kirk, R.L., 2008. Recent bright gully deposits on Mars: Wet or dry flow?
889 *Geology* 36, 211. <https://doi.org/10.1130/G24346A.1>
- 890 Prancevic, J.P., Lamb, M.P., 2015. Particle friction angles in steep mountain channels: Friction angles in mountain
891 channels. *J. Geophys. Res. Earth Surf.* 120, 242–259. <https://doi.org/10.1002/2014JF003286>
- 892 Python, 2021. Python packages OpenCV and TrackPy.
- 893 Quartier, L., Andreotti, B., Douady, S., Daerr, A., 2000. Dynamics of a grain on a sandpile model. *Phys. Rev. E* 62,
894 8299–8307. <https://doi.org/10.1103/PhysRevE.62.8299>
- 895 Rapp, A., 1960. Talus slopes and mountain walls at Tempelfjorden, Spitsbergen (No. 96), Norsl Polarinstitut
896 Skrifter. University of Oslo, Oslo.
- 897 Sass, O., Krautblatter, M., 2007. Debris flow-dominated and rockfall-dominated talus slopes: Genetic models
898 derived from GPR measurements. *Geomorphology* 86, 176–192.
899 <https://doi.org/10.1016/j.geomorph.2006.08.012>
- 900 Scheingross, J.S., Brun, F., Lo, D.Y., Omerdin, K., Lamb, M.P., 2014. Experimental evidence for fluvial bedrock
901 incision by suspended and bedload sediment. *Geology* 42, 523–526. <https://doi.org/10.1130/G35432.1>
- 902 Selby, M.J., 1982. *Hillslope Materials and Processes*. Oxford University Press, Oxford, UK.
- 903 Shinbrot, T., Duong, N.-H., Kwan, L., Alvarez, M.M., 2004. Dry granular flows can generate surface features
904 resembling those seen in Martian gullies. *Proc. Natl. Acad. Sci.* 101, 8542–8546.
905 <https://doi.org/10.1073/pnas.0308251101>
- 906 Shugar, D.H., Jacquemart, M., Shean, D., Bhushan, S., Upadhyay, K., Sattar, A., Schwanghart, W., McBride, S., de
907 Vries, M.V.W., Mergili, M., Emmer, A., Deschamps-Berger, C., McDonnell, M., Bhambri, R., Allen, S.,
908 Berthier, E., Carrivick, J.L., Clague, J.J., Dokukin, M., Dunning, S.A., Frey, H., Gascoin, S., Haritashya,
909 U.K., Huggel, C., Kääh, A., Kargel, J.S., Kavanaugh, J.L., Lacroix, P., Petley, D., Rupper, S., Azam, M.F.,
910 Cook, S.J., Dimri, A.P., Eriksson, M., Farinotti, D., Fiddes, J., Gnyawali, K.R., Harrison, S., Jha, M.,
911 Koppes, M., Kumar, A., Leinss, S., Majeed, U., Mal, S., Muhuri, A., Noetzli, J., Paul, F., Rashid, I., Sain,
912 K., Steiner, J., Ugalde, F., Watson, C.S., Westoby, M.J., 2021. A massive rock and ice avalanche caused
913 the 2021 disaster at Chamoli, Indian Himalaya. *Science* 373, 300–306.
914 <https://doi.org/10.1126/science.abh4455>
- 915 Sklar, L.S., Dietrich, W.E., 2004. A mechanistic model for river incision into bedrock by saltating bed load. *Water*
916 *Resour. Res.* 40. <https://doi.org/10.1029/2003WR002496>
- 917 Sklar, L.S., Dietrich, W.E., 2001. Sediment and rock strength controls on river incision into bedrock 4.
- 918 Stock, G.M., B.D., C., Santaniello, D.J., Zimmer, V.L., Wiczorek, G.F., Snyder, J.B., 2013. Historical Rock Falls
919 in Yosemite National Park, California (1857–2011) (No. 746), U.S. Geological Survey Data Series.
- 920 Sun, Z., Ulizio, T.P., Fischer, J.N., Levin, J.N., Beer, A.R., Dickson, J.L., Lamb, M.P., 2021. Formation of low-
921 gradient bedrock chutes by dry rockfall on planetary surfaces. *Geology*.
- 922 Turowski, J.M., Wyss, C.R., Beer, A.R., 2015. Grain size effects on energy delivery to the streambed and links to
923 bedrock erosion. *Geophys. Res. Lett.* 42, 1775–1780. <https://doi.org/10.1002/2015GL063159>
- 924 Vijayan, S., Harish, Kimi, K.B., Tuhi, S., Vigneshwaran, K., Sinha, R.K., Conway, S.J., Sivaraman, B., Bhardwaj,
925 A., 2022. Boulder Fall Ejecta: Present Day Activity on Mars. *Geophys. Res. Lett.* 49.
926 <https://doi.org/10.1029/2021GL096808>
- 927 Volkwein, A., Schellenberg, K., Labiouse, V., Agliardi, F., Berger, F., Bourrier, F., Dorren, L.K.A., Gerber, W.,
928 Jaboyedoff, M., 2011. Rockfall characterisation and structural protection – a review. *Nat. Hazards Earth*
929 *Syst. Sci.* 11, 2617–2651. <https://doi.org/10.5194/nhess-11-2617-2011>
- 930 Ward, D.J., Berlin, M.M., Anderson, R.S., 2011. Sediment dynamics below retreating cliffs: SEDIMENT
931 DYNAMICS BELOW RETREATING CLIFFS. *Earth Surf. Process. Landf.* 36, 1023–1043.
932 <https://doi.org/10.1002/esp.2129>
- 933 Wiczorek, G.F., Snyder, J.B., Alger, C.S., Isaacson, K.A., 1992. Rock falls in Yosemite Valley, California (Open-
934 File Report 92-387), Open-File Report. National Park Service, Yosemite National Park, California.
- 935 Williams, J.G., Rosser, N.J., Hardy, R.J., Brain, M.J., 2019. The Importance of Monitoring Interval for Rockfall
936 Magnitude-Frequency Estimation. *J. Geophys. Res. Earth Surf.* 124, 2841–2853.
937 <https://doi.org/10.1029/2019JF005225>

- 938 Williams, S.G.W., Furbish, D.J., 2021. Particle energy partitioning and transverse diffusion during rarefied travel on
939 an experimental hillslope. *Earth Surf. Dyn.* 9, 701–721. <https://doi.org/10.5194/esurf-9-701-2021>
- 940 Wright, V., Dasent, J., Kilburn, R., Manga, M., 2022. A Minimally Cemented Shallow Crust Beneath InSight.
941 *Geophys. Res. Lett.* 49. <https://doi.org/10.1029/2022GL099250>
- 942 Xiao, Z., Zeng, Z., Ding, N., Molaro, J., 2013. Mass wasting features on the Moon – how active is the lunar surface?
943 *Earth Planet. Sci. Lett.* 376, 1–11. <https://doi.org/10.1016/j.epsl.2013.06.015>
- 944 Yuanlin, Z., Carbee, D.L., 1987. Tensile strength of frozen silt 30.

945

946 **Table 1: Outline of the dry grain abrasion experiments**, ordered by flume slope angle. Each experiment's data
 947 symbol (as used in Figure 5, Figure 6, and Figure S4) refers to the relative size and shape of the used grains (large
 948 vs. small, and round vs. angular). Erodible-bed experiments (*EB*) are denoted with grey background shading, and
 949 fixed-bed experiments (*FB*) are of white background. More detailed measurements of the erodible bed experiments
 950 *EB* are given in Table S2.

951 **Figure 1: Concept of rocky hillslope abrasion by dry rockfall:** Exemplary erosional rocky hillslope topography:
 952 (A) plinth bedrock below a sandstone cap (Marble Canyon, AZ, USA), (B) chute channel in a basaltic lava flow
 953 (Pan de Azúcar National Park, Chile), (C) basaltic bedrock gullies on Dawes crater walls on the Moon (Kumar et al.,
 954 2013), and (D) furrowed Basalt bedrock gullies on Endurance Crater wall on Mars (google Mars). Exemplary sites
 955 of dry grain transport over underlying (E) granular substrate and (F) over bedrock substrate, San Gabriel
 956 Mountains, CA. Conceptual sketches illustrate hillslope morphologies resulting from dry grain transport and erosion
 957 over (G) gravel substrate and (H) over bedrock substrate.

960 **Figure 2: Dry grain abrasion model setup and experimental scheme:** (A) definitions of grain trajectory variables
 961 in the dry grain abrasion model (DGAM; model scheme in Table S1; see notation section), (B) schematic of the
 962 tilted flume filled with PU foam, sediment feeding and collection, terrestrial laser scanner (TLS) positions and
 963 visual fields of particle imaging velocimetry (PIV), (C) picture in horizontal view on an initial smooth flume foam
 964 surface, and (D) sample set of used dry, rounded rhyolite grains of $d_{grain} = 0.03m$.

966 **Figure 3: Abraded surface patterns of the erodible-bed experiments (EB):** (A) evolution of the foam surface
 967 during *EB5* given at three temporal states, as indicated by the total grain mass run through until then ($m_{grains,tot}$).
 968 Color code is for vertical surface abrasion (note different range per panel). Contours denote abrasion depths in steps
 969 of grain size ($d_{grain} = 1.5cm$). The cleft to the bottom left in the central panel is an artifact due to missing surface
 970 data. Three lateral (cross sections, cs) and one central long profile through the evolving surface of *EB5* are shown in
 971 Figure 4A to C. (B) Grey-shaded surface meshes of the grain entrance area at the final experimental states, resulting
 972 from different flume slope angles, grain sizes, and grain feed configurations: equal feed over the whole flume width
 973 (*EB1* and *EB2*), central feed (*EB3* and *EB4*), and pointwise feed (*EB5*; cf. Table S2). Grain feed entrance directions
 974 are indicated by the arrows, and flume constrictions for *EB3* and *EB4* are visible by the vertical black boards,
 975 respectively. The upper flume bed section visible in (B) consisted of a fixed (non-abradable) board. Parallel blue
 976 lines are horizontal (lateral) contours in 0.05m spacing, and yellow lines are vertical contours in 0.01m spacing.

977 **Figure 4: Transient topographic evolution of an erodible-bed experiment (EB5):** (A) cross sections through the
 978 flume showing bed elevation below the initial surface for three experimental times and at three positions down the
 979 flume (cs1=0.3m, cs2=0.65m, and cs3=1.25m; see Figure 3A left panel), (B) relative distribution of grains passing
 980 through these cross sections around the three experimental times, (C) mean abrasion depth per grain impact on a
 981 quadratic grain footprint (equals w_{cell} in the DGAM model), and (D) central long profile evolution down the flume
 982 shown for several experimental times with indicated evolving topographic features (cf. Figure 3A right panel).

984 **Figure 5: Grain trajectory statistics of the experiments:** (A) a grain hop length l_{hop} , (B) grain hop height h_{hop} ,
 985 (C) grain impact angle α_{in} , and (D) grain impact velocity v_{in} against flume slope angle θ_{slope} . Boxplots show
 986 statistics given as described in the inset in (C). Data from the erodible-bed experiments (*EB1-EB3* and *FB5*) is
 987 shown with grey shading, and data from fixed-bed experiments are of white background (*FB1-FB6*). Grain shapes
 988 and relative grain sizes of the experiments are indicated as symbols above (A), (cf. symbol assignments in Table 1,
 989 upper part). The mean values indicated by the dotted lines (\bar{l}_{hop} , \bar{h}_{hop} , $\bar{\alpha}_{in}$, and \bar{v}_{in}) refer to the erodible-bed
 990 experiments only, since the fixed-bed experiments likely started with higher initial grain velocities.

993 **Figure 6: Mean impact abrasion and grain erosivity of the erodible-bed experiments (EB) varying flume slope
 994 angle:** (A) mean vertical impact abrasion, w_{cell} (i.e., abrasion volume of an impacting grain, V_{cell} , divided by cell
 995 area $d_{cell}^2 = d_{grain}^2$; Equation 9), (B) abrasion volume, V_{cell} , divided by the surface-normal component of the grain's
 996 impact energy, $\varepsilon_{in,n}$, called grain erosivity, k_{ero} , and (C) these values further divided by the impacting grain's cross-
 997 sectional area $d_{cell}^2 = d_{grain}^2$ with two labeled values for rounded and angular grains, respectively. Relative symbol
 998 size and shape are defined by used grain size and grain shape of the erodible-bed experiments (*EB*, symbols assigned
 999 in Table 1, upper part). The grey-shaded area in the background denotes the common span for the angle of repose
 1000 for grain piles.

1001
 1002 **Figure 7: Calibration of the DGAM model by selecting the shock term:** Predicted mean grain trajectory
 1003 variables divided by measured mean trajectory variables for erodible-bed experiment 2 (*EB2*), plotted against the
 1004 shock term (κ_{shock}), which was varied in the modeling in steps of 0.1m^{-1} . Unity on the y-axis means ideal model-
 1005 reproduction of the measurements. The selected shock term (indicated by the vertical dotted line) was chosen at the
 1006 first closest general agreement.

1007
 1008 **Figure 8: Reproduction of erodible-bed experiment (*EB*) grain trajectories with DGAM:** PIV-measured
 1009 trajectory data and calibrated DGAM predictions along the flume for (A) grain hop length, l_{hop} , (B) grain impact
 1010 velocities, v_{in} , (C) surface-normal grain impact velocity components, $v_{in,n}$, (D) grain deflection velocities, v_{out} , (E)
 1011 absolute grain impact angles, α_{in} , (F) absolute grain deflection angles, α_{out} , and (G) grain impact cell abrasion
 1012 volume, V_{cell} . Shown are measured PIV data for the fields of view of the three lateral PIV cameras (boxplots with
 1013 median in grey, box-size of 50% interquartile range and whisker length of 1.5 times thereof, for data over 5cm bins
 1014 downslope the flume) and mean DGAM predictions for 280 grains, equally sourced across the modeled flume width
 1015 (black triangles). Data from erodible-bed experiment 2 (*EB2*; Table 1), PIV-camera positions are shown in Figure
 1016 2B.

1017
 1018 **Figure 9: Parameter space exploration for DGAM:** Model predictions vs. experimental data for (A) varying slope
 1019 angle, θ_{slope} , and keeping grain size constant ($d_{grain} = 0.03\text{m}$), and (B) varying grain size, d_{grain} , and keeping
 1020 slope angle constant ($\theta_{slope} = 35^\circ$), respectively. Experimental PIV data is from the erodible-bed experiments (*EB*,
 1021 boxplots with whiskers extending to 1.5 times the interquartile range from the box), and mean PIV data is from the
 1022 fixed-bed experiments (*FB*, diamonds; Table 1). DGAM-predictions in (A) based on the erosivity-calibration for
 1023 round grains (following the normalized grain erosivity 0.001m/J in Figure 6C; bold blue lines), representative for
 1024 *EB3*, *EB4*, and *FB1-FB6*, while prediction for angular grains measured on another grain size is shown for
 1025 comparison (normalized erosivity 0.003m/J , *EB5* and thin yellow lines). DGAM-predictions in (B) based on
 1026 erosivity-calibration for angular grains, representative for *EB5* and *FB4* (bold yellow lines), while prediction for
 1027 round grains measured on another slope angle is shown for comparison (*EB3* and thin blue lines). The panels per
 1028 row show grain hop length, l_{hop} , grain impact velocity, v_{in} , grain impact angles, α_{in} , volumetric grain impact
 1029 abrasion, V_{cell} , and local impact abrasion (i.e. V_{cell} divided by mean hop length, l_{hop}), respectively. Abrasion for the
 1030 fixed-bed experiments (*FB*, diamonds) was not measured but predicted based on the erodibility of experiment *EB3*.
 1031

1032 **Figure 10: Predicted transient hillslope channelization varying rockfall grain feed:** Simulations used varied
 1033 grain feed patterns: (A) uniform central feed over 10 model cells, and (B) uniform feed in three inlets of 3, 4 and 3
 1034 cell widths (as indicated by the blue arrows on top of the third panels). DGAM-calibration was for erodible-bed
 1035 experiment 2 (*EB5*; Table 1) with fixed $m_{grains,tot} = 800\text{tons}$ of angular $d_{grain} = 0.20\text{m}$ grains (normalized
 1036 erosivity 0.003m/J ; cf. Figure 6C) and a hillslope angle of $\theta_{slope} = 35^\circ$. Shown are stacked cross-sections (cs)
 1037 through the transiently abraded hillslopes in a horizontal perspective, with initial (dotted), intermediate (i.e., half-
 1038 time; grey), and final topography (black), respectively (more cross-sections are given in Figure S3). The lowest
 1039 panels of (A) and (B) additionally show the transient lateral distribution of passing grains down the whole slope for
 1040 the three experimental times (normalized number of transported grains; bin width is 0.2m). (C) and (D) show the
 1041 central long profiles (lp) for both simulations with evolving troughs and rims; the position of the cross-sections of
 1042 (A) and (B) are also indicated. Modeled topographies in panels (A, B) are comparable to the experimental
 1043 topographies in Figure 4A and B, long profiles in panels (C, D) are comparable to Figure 4D.

1044

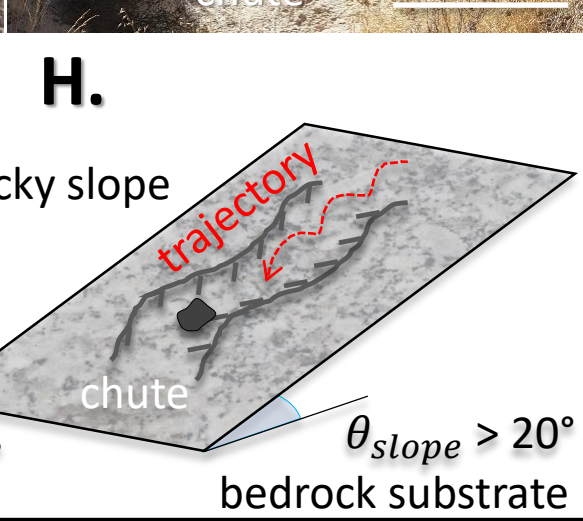
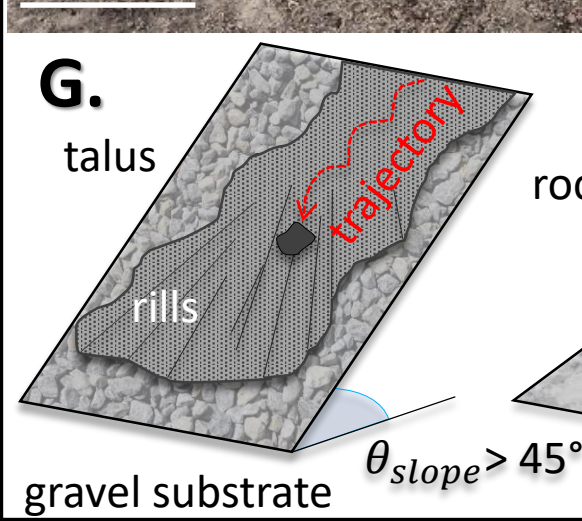
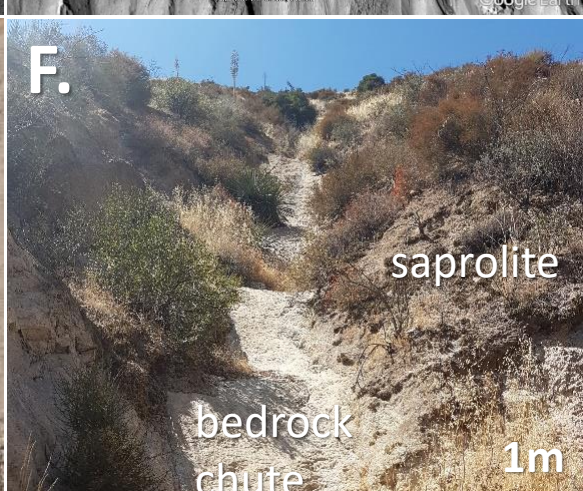
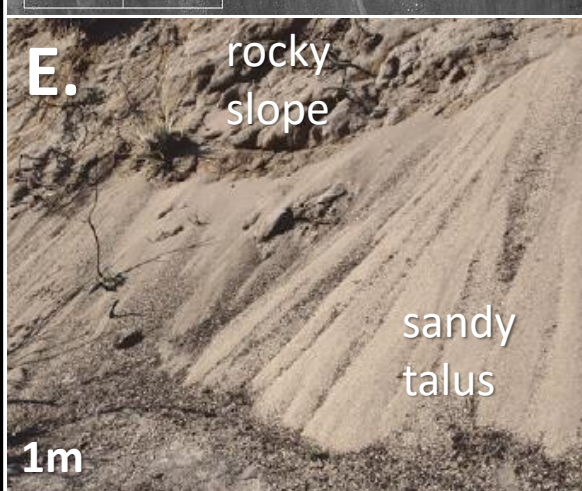
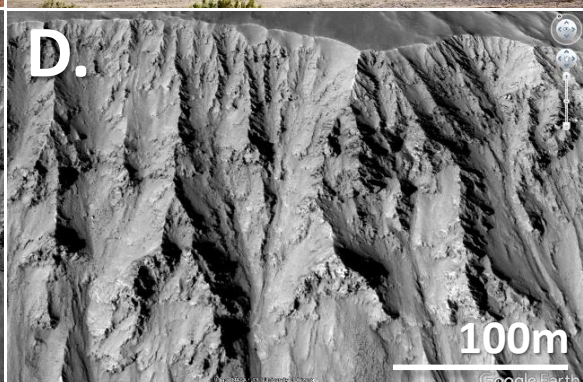
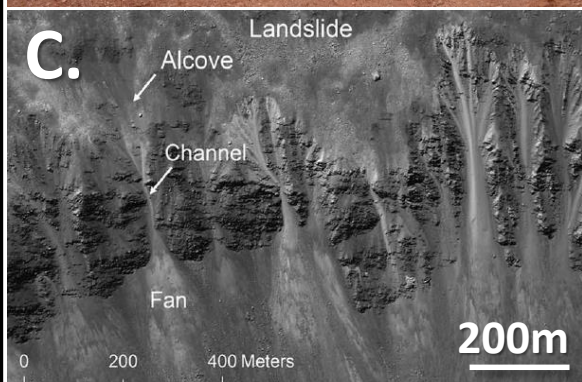
| experiments | | | flume | dry grain properties | | | | | grain trajectory statistics [†] | | | foam abrasion | | |
|-------------------------|-----------|---|-----------------------------|----------------------|-----------|--------------------------|----------------------------|-----------------------|---|--|---------------------------------|-----------------------------|--|--|
| erodible-bed | fixed-bed | symbol in Figures | slope, Θ_{slope} [°] | type | shape | surface friction | pocket friction | size, d_{grain} [m] | total grain mass, $m_{grains,tot}$ [tons] | relative impact angle [#] , α_{in} [°] | impact velocity, v_{in} [m/s] | hop distance, l_{hop} [m] | total abrasion volume, V_{flume} [m ³] | grain impact erosivity, k_{ero} [cm ³ /J] |
| | | | | | | angle, Φ_{surf} [°] | angle, Φ_{pocket} [°] | | | | | | | |
| <i>EB1</i> [*] | |  | 16.7 | Granite | | 20 | 34 | 0.061 | 22.5 | 9.5 | 1.1 | 0.16 | 0.090 | 2.65 |
| <i>EB2</i> | |  | | | rounded | | 34.7 | 0.023 | 8.3 | 9.0 | 1.2 | 0.11 | 0.046 | 1.00 |
| <i>EB3</i> | |  | 19.5 | Andesite (tumbled) | | 23.5 | 40.3 | 0.030 | 2.7 | 9.8 | 1.8 | 0.09 | 0.013 | 0.30 |
| <i>EB4</i> | |  | | | | | | | 5.1 | 10,5 [^] | 0,8 [^] | 0,07 [^] | 0.017 | 1.38 |
| <i>EB5</i> | |  | 35.0 | Granite | angular | 33.4 | 55.6 | 0.015 | 16.5 | 10.5 | 1.6 | 0.16 | 0.040 | 0.68 |
| <i>FB1</i> | |  | 20 | | | | | | | 6.0 | 1.9 | 0.13 | - | - |
| <i>FB2</i> | |  | 25 | | | | | | | 16.9 | 2.1 | 0.20 | - | - |
| <i>FB3</i> | |  | 30 | Andesite | rounded | | | | | 2,7 [^] | 2,2 [^] | 0,22 [^] | - | - |
| <i>FB4</i> | |  | 35 | | (tumbled) | 23.5 | 44.4 | 0.036 | 2.6e-4 | 19,1 [^] | 2,5 [^] | 0,32 [^] | - | - |
| <i>FB5</i> | |  | 40 | | | | | | | 29.8 | 2.4 | 0.23 | - | - |
| <i>FB6</i> | |  | 45 | | | | | | | 35.5 | 2.7 | 0.24 | - | - |

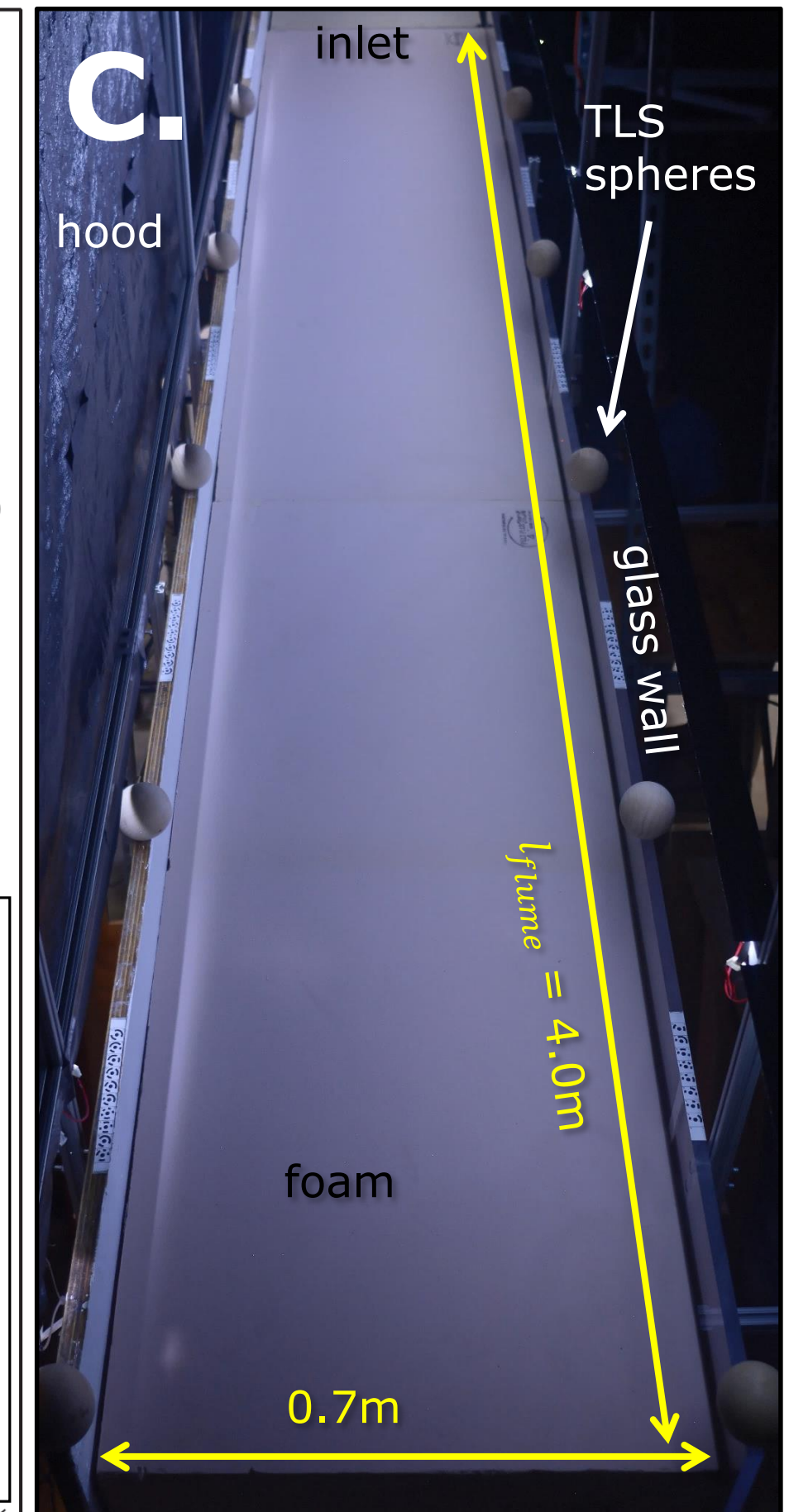
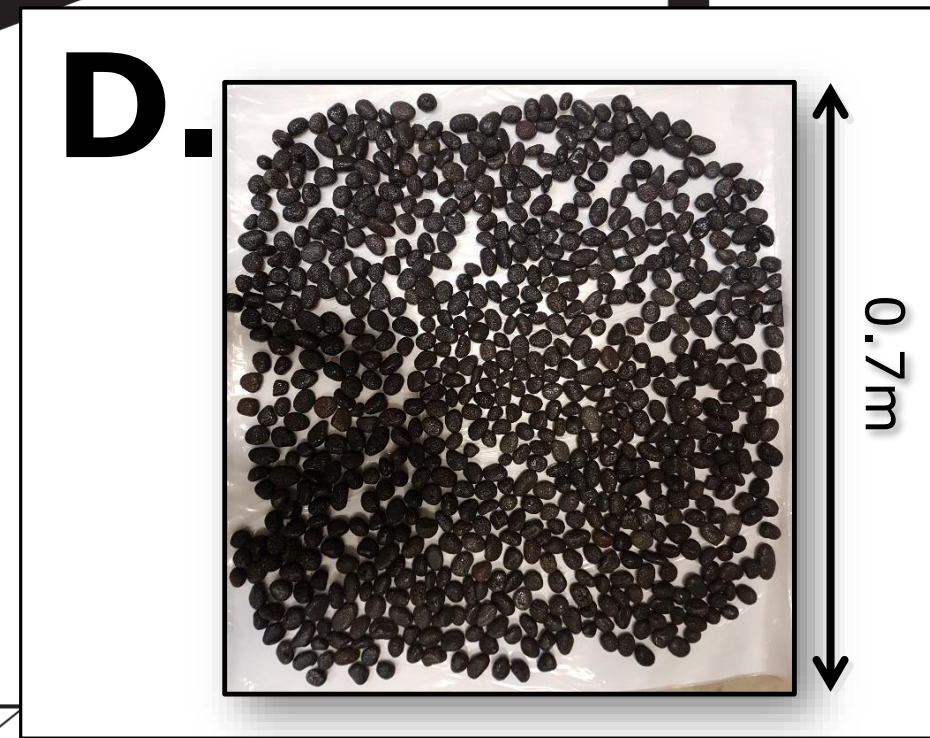
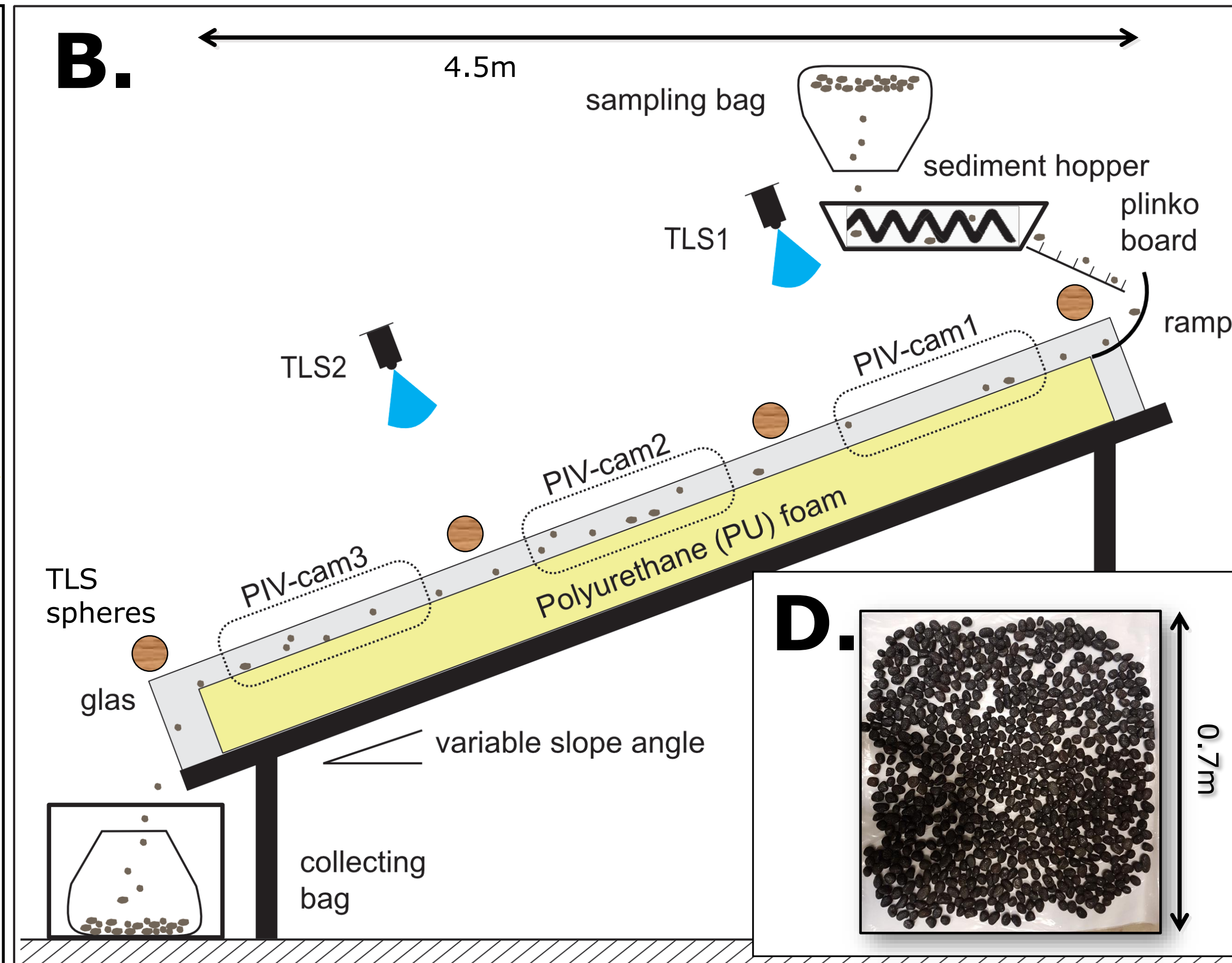
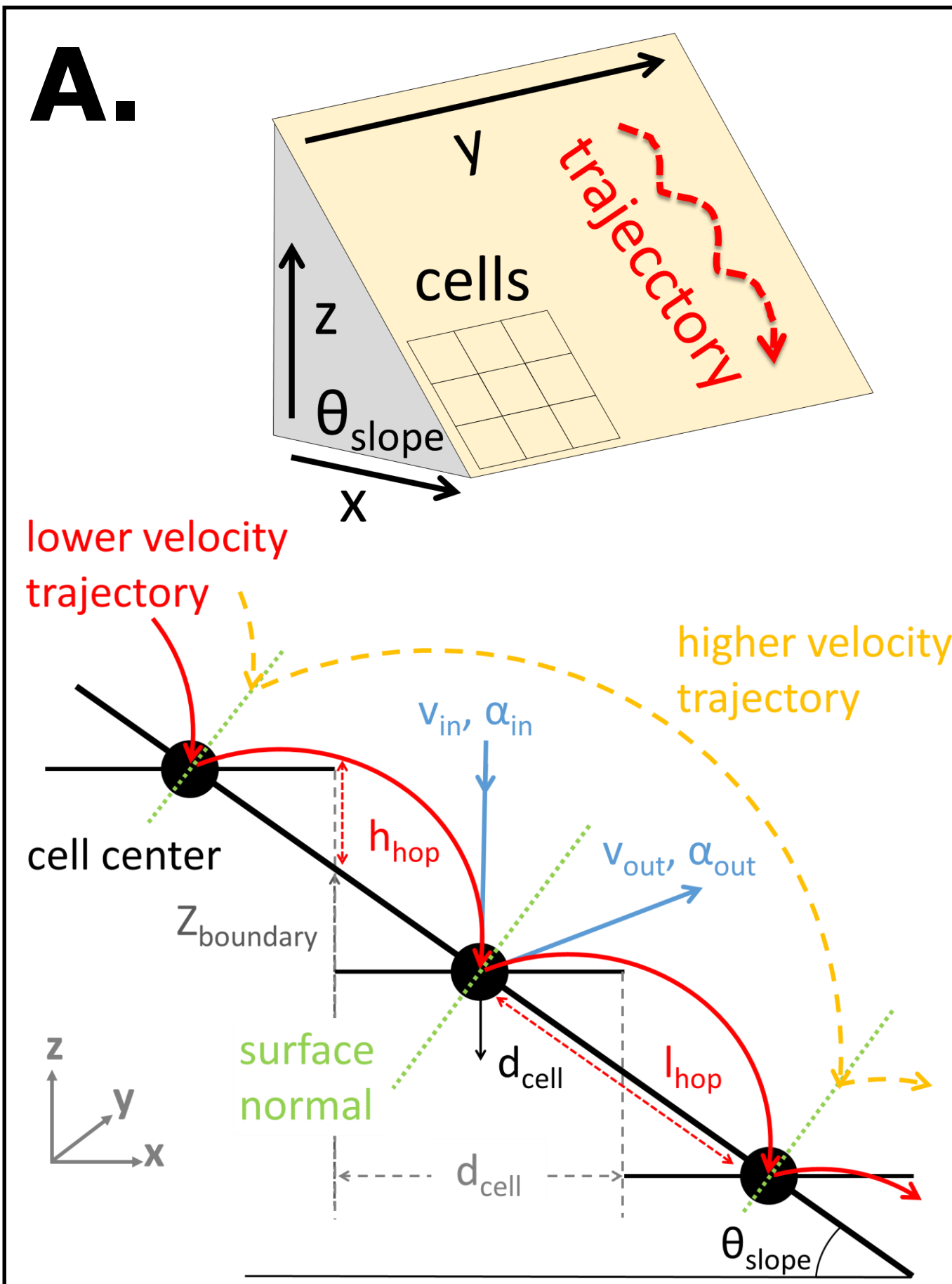
* data from Sun et al., 2021

[†] data from the second lateral camera (i.e. PIV-cam2, central along the flume, neither at the inlet nor at the outlet; Figure 2B)

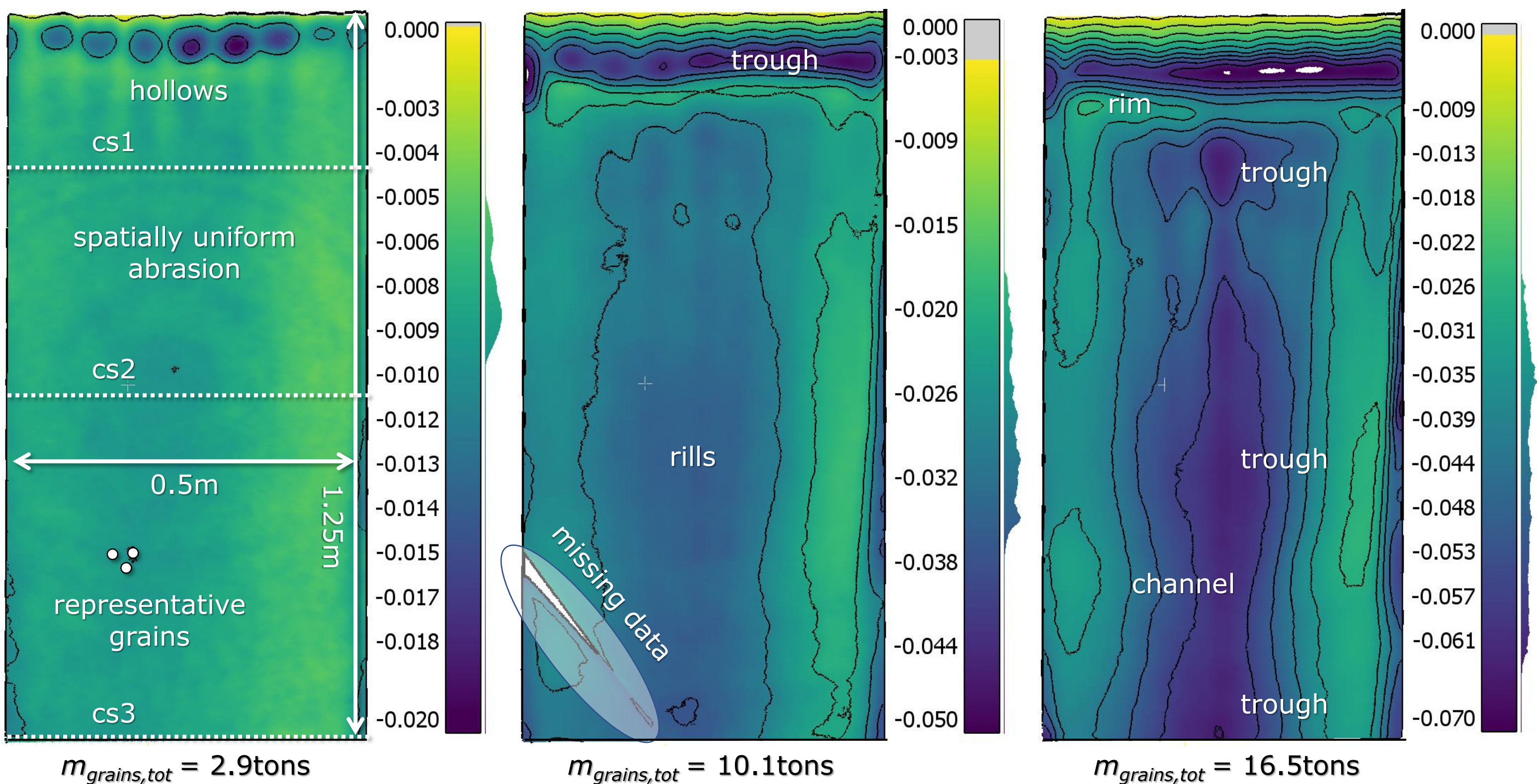
[#] angles are relative to the flume surface (i.e. they are not corrected for the flume slope Θ_{slope})

[^] uncertain data (few measurements)





A. transient topography of *EB5*



B. final erodible-bed topographies

